ORIGINAL PAPER

Serpentinization of New Caledonia peridotites: from depth to (sub-)surface

Marc Ulrich[1] · Manuel Muñoz[2] · Philippe Boulvais[3] · Michel Cathelineau[4] · Dominique Cluzel[5] · Stéphane Guillot[6] · Christian Picard[7]

Abstract

Serpentinization processes occur at geological settings notably during oceanic subduction and obduction, where mantle rocks interact with water. Different types of serpentine minerals form according to temperature and pressure conditions, and potentially chemical exchanges. Therefore, the characterization of serpentine minerals, and the possible occurrence of multiple serpentine generations in mantle rocks provide essential constraints on the conditions of fluid–rock interactions in the mantle. The serpentinite sole of the Peridotite Nappe of New Caledonia (Southwest Pacific) is the result of several superimposed serpentinisation events. The latter were discriminated using mineralogical and geochemical approaches and modeling. Lizardite represents more than 80% of the entire serpentine content of the ophiolite. It is crosscut by several veins of other serpentine species in the serpentinite sole. The relative chronology appears as follows: lizardite 1 → lizardite 2 → antigorite → chrysotile → polygonal serpentine. The transition from primary/magmatic minerals to lizardite 1 is almost isochemical. Then, the development of lizardite 2 yields an enrichment in fluid-mobile elements such as Cs, Rb, Ba, U and light rare-earth elements and an apparent increase of the Fe^{3+}/Fe_T ratio. The modeling of $\delta^{18}O$ values (1.9–13.9‰) and δD values (88–106‰) of all serpentine species through Monte-Carlo simulations show that New Caledonia serpentines were mainly formed in equilibrium with fluids released by the dehydration of altered oceanic crust (AOC) during subduction between 250 and 350 °C. AOC-derived fluids are not the unique source of fluids since a low temperature (100–150 °C) meteoric component is also predicted by the models. Thus, serpentine acts as a tape-recorder of fluid–rock interactions into the mantle from depth to (sub-)surface.

✉ Marc Ulrich
mulrich@unistra.fr

1 Université de Strasbourg, CNRS, IPGS, UMR 7516, 67000 Strasbourg, France

2 Géosciences Montpellier, University Montpellier, CNRS, Montpellier, France

3 Géosciences Rennes-UMR 6118, University Rennes, CNRS, 35000 Rennes, France

4 Georessources CNRS UMR 7566, Vandœuvre-lès-Nancy, France

5 ISEA, Université de La Nouvelle-Calédonie, BP R4, 98851 Nouméa Cedex, New Caledonia

6 University Grenoble Alpes, University Savoie Mont Blanc, CNRS, IRD, IFSTTAR, ISTerre, 38000 Grenoble, France

7 Laboratoire Chrono-Environnement CNRS UMR 6249, Besançon, France

Introduction

Serpentinization is a hydrothermal alteration process that leads to upper mantle hydration. Serpentine minerals are ubiquitous in ultramafic rocks from various geological settings and their crucial role in tectonic and chemical processes has been widely documented over the past

two decades: In divergent environments, which include ultraslow and slow-spreading centers and mantle-exhuming passive margins, serpentine occurs mainly along fractures and detachment faults, weakening the upper mantle, promoting strain localization and resulting in the exhumation of serpentinized peridotites at the seafloor (Andréani et al. 2007, 2014; Cannat et al. 1995; Chenin et al. 2017; Delacour et al. 2008; Gillard et al. 2019; Guillot et al. 2015; Mével 2003; Picazo et al. 2012). Such tectonic processes involve significant mass transfer between the mantle and oceanic reservoirs (Alt and Shanks III 2003; Iyer et al. 2008; Kodolanyi et al. 2012; Pinto et al. 2016; Rouméjon et al. 2015; Schwarzenbach et al. 2015). Also, the rheology of serpentinized rocks strongly influences deformation and seismicity in the forearc and controls geodynamics of the subduction zone (Hyndman and Peacock 2003; Peacock and Hyndman 1999; Stern 2002). Here again, serpentine is assumed to be one of the most efficient ways to recycle water and fluid-mobile elements (FME) into the deeper mantle (Debret et al. 2013; Deschamps et al. 2011, 2012; Klein et al. 2017; Poli and Schmidt 2002; Rüpke et al. 2004; Savov et al. 2005; Scambelluri et al. 2004). Thus, the uppermost part of the oceanic lithosphere is hydrothermally altered before entering subduction zones. Then, the dehydration of the subducting slab favors the formation of forearc serpentine, which hosts a large amount of water (up to ~ 13 wt%). The circulation of such an amount of aqueous fluids may, in turn, transport fluid-mobile elements (FME) deep into the mantle down to ~ 150 km (Ulmer and Trommsdorff 1995; Wunder et al. 2001). At temperature above ~ 650 °C, serpentine is no longer stable and aqueous fluids are liberated by serpentine breakdown, triggering mantle wedge melting that gives rise to arc volcanism (Hattori and Guillot 2003; Iwamori 1998; Reynard 2013; Schmidt and Poli 1998; Ulmer and Trommsdorff 1995, 1999). Therefore, studying serpentinite is fundamental in the aim of addressing questions about plate tectonics and global geochemical cycles.

When convergence results in the closure of ocean basins, slices of the forearc mantle may be obducted. Serpentinite then acts as a lubricant, facilitating the ophiolite emplacement and subsequent exhumation of the high pressure rocks (Agard et al. 2016; Guillot et al. 2000, 2009; Schwartz et al. 2001). However, the conditions of fluid–rock interactions and serpentine formation, as well as the nature and source of serpentinizing fluids, are mostly unconstrained.

In New Caledonia (NC), large ultramafic massifs form an extensive and well-exposed ophiolite obducted during the Late Eocene, termed Peridotite Nappe (Fig. 1; Avias 1967). Peridotites recorded various degrees of serpentinization, and the base of the Peridotite Nappe is made of a thick serpentinite sole characterized by multiple generations of serpentine veins, the origin of which remains unclear (Frost et al. 2013; Gautier et al. 2016; Mothersole et al. 2017; Quesnel

et al. 2016b; Ulrich et al. 2014). In this paper, the source and nature of the fluids involved in the serpentinization are therefore unraveled thanks to new petrological, mineralogical and geochemical data as well as geochemical modeling.

Geological settings

New Caledonia is an island of the SW Pacific, ~ 1300 km to the east of Australia, which forms the northernmost part of the Norfolk Ridge, an elongated slice of thinned and largely submarine continental crust, rifted from the Gondwana margin during the Late Cretaceous. The Peridotite Nappe tectonically overlies a patchwork of pre-Oligocene terranes and covers at present about one-third of the island. The main unit is located in the south of the island, so-called Massif du Sud, and several tectonic klippes are spread along the West coast (Fig. 1). All these units result from the evolution of a marginal basin that opened to the east of the Norfolk Ridge during the Campanian–Paleocene (90–55 Ma; Cluzel et al. 2001). This basin was inverted at 56 Ma by northeastward-subduction (Cluzel et al. 2012a) and the upper plate of the system (the Loyalty Basin) was obducted at ca. 34 Ma (Cluzel et al. 1998) when the Norfolk ridge entered the trench and jammed the Eocene subduction. Harzburgites and dunites formed in a supra-subduction zone environment are predominant, while lherzolites, inherited from the initial marginal basin are also found in the northernmost massifs (Pirard et al. 2013; Secchiari et al. 2016, 2019; Ulrich et al. 2010). The Peridotite Nappe bears a lateritic regolith (up to 100 m thick) that contains ~ 10% of the world Ni reserves (McRae 2018). The Peridotite nappe overlies the Poya Terrane, which corresponds to a large composite allochthon formed of two sub-units: (i) tectonic slices of massive and pillow basalt (Poya Terrane Basalts) of dominant MORB affinity and abyssal argillites of Campanian to Early Eocene age (Aitchison et al. 1995), derived from the upper oceanic crust of the South Loyalty Basin (Cluzel et al. 1997; Eissen et al. 1998) and accreted in the fore-arc region of the Loyalty Arc (Cluzel et al. 2001), and (ii) Coniacian–Santonian distal turbidites (Kone Facies) accumulated on the ancient passive margin of the Norfolk Ridge, and intruded by lower Eocene dolerite sills of EMORB affinity (Cluzel et al. 2018).

The serpentinization processes of the Peridotite Nappe have never been studied in-depth, while peridotites are highly serpentinized. Orloff (1968) highlighted, for the first time, the decreasing degree of serpentinization from bottom to the top of the ophiolite. More recently, Frost et al. (2013) identified three generations of serpentine veins in a dunite sample: two-first generations of lizardite and the last one of chrysotile. The transformation of lizardite to chrysotile would have been accompanied by the release of Fe and the subsequent formation of magnetite. Mothersole et al. (2017)
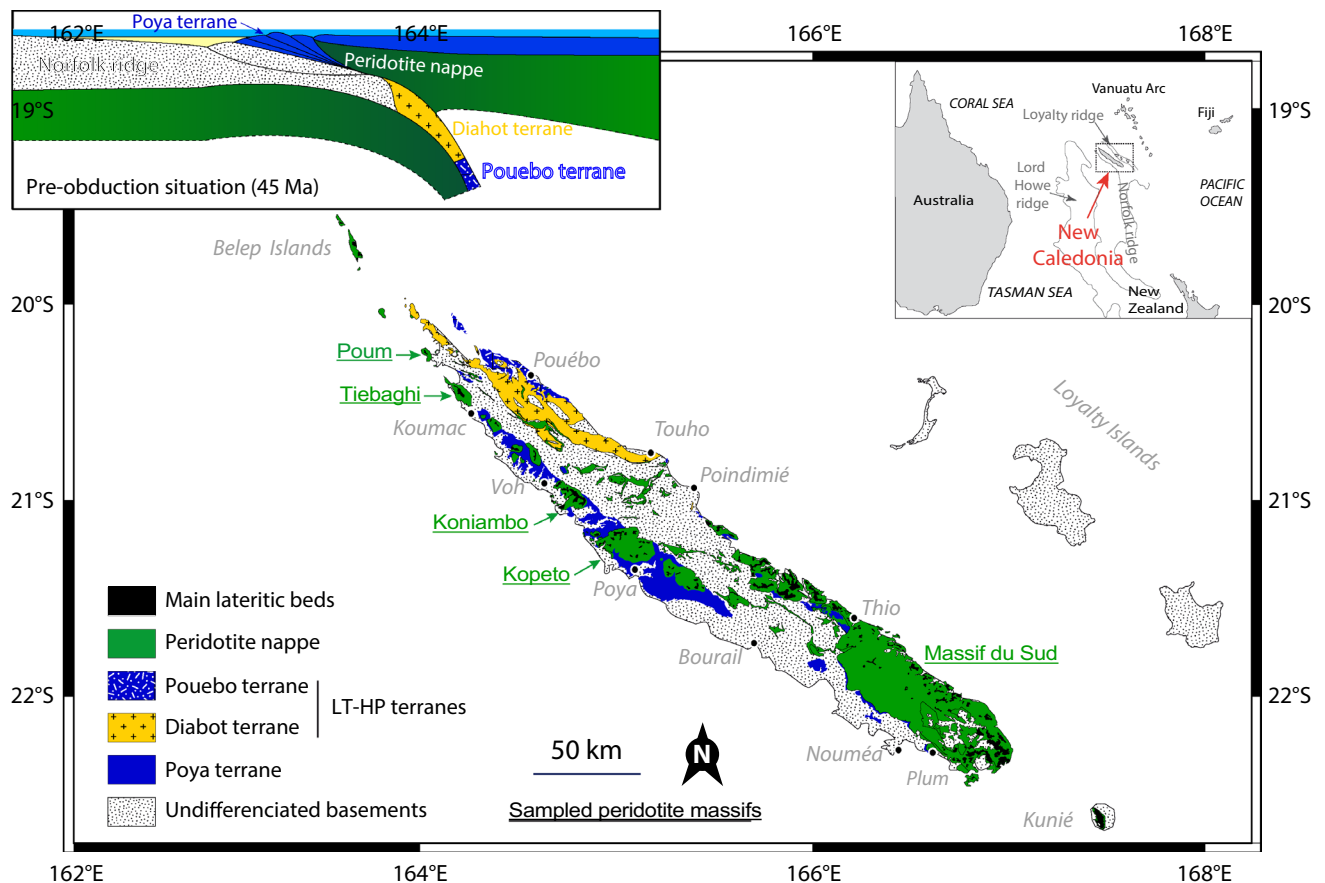
Fig. 1 Simplified geological map of New Caledonia, showing the exposures of Paleocene-Eocene terranes, (adapted from Maurizot). Pre-obduction situation is modified from Cluzel et al. (2012a,b)

used NC serpentinites as proxies of mantle wedge serpentinites and compared them with those from the 15′20° N fracture zone in the Mid-Atlantic Ridge to evaluate the effect of hydrothermal alteration on a budget of major and minor elements in the two different geodynamic settings (Mothersole et al. 2017). They concluded that serpentinization was nearly identical in the two environments, except more oxidized Fe as well as enrichments in Cl, S, and C in abyssal serpentinites compared to the forearc serpentinites. Serpentine-bearing faults were extensively studied (i) to characterize their kinematics and the mechanisms of NC ophiolite emplacement on the continental basement (Gautier et al. 2016; Quesnel et al. 2016b), and (ii) to constrain the carbonation and silicification of the serpentinite sole in relation to meteoric fluid percolation (Quesnel et al. 2013,2016a; Ulrich et al. 2014) and (iii) to understand the formation of secondary Ni-rich phyllosilicates, mostly talc-like phases, in serpentine-filled fractures at the top of the ophiolite (Cathelineau et al. 2015,2016; Fritsch et al. 2016; Muñoz et al. 2019). High temperature, slab-derived fluids are proposed for the origin of syntectonic tremolite–antigorite veins, which are widespread in the Peridotite Nappe (Cluzel et al.

2019). But the source and nature of fluids in equilibrium with the main serpentinization episode that affected the whole ophiolite remains, however, unconstrained.

Materials and methods

Sampling and analytical strategies

A collection of 30 samples, collected from 5 different massifs (the Massif du Sud, Kopeto, Koniambo, Tiébaghi and Poum), includes serpentinized harzburgites, lherzolites and dunites referred to as "upper serpentine" hereafter, as well as serpentinites from the sole of the Peridotite Nappe. They represent most rock types and serpentine occurrences of the NC ophiolite.The serpentinites were characterized by: (1) Raman spectroscopy, to identify serpentine species, (2) major and trace element chemistry of primary minerals and serpentines crystals, to evaluate the chemical mobility during fluid–rock interactions, (3) oxygen and hydrogen isotope geochemistry of each serpentine variety to discuss the source of fluids involved in the serpentinization processes.

Raman spectroscopy

Raman spectra were acquired at ENS Lyon (France) using a Horiba Jobin–Yvon LabRam HR800 spectrometer and a visible ionized argon laser source with a wavelength of 514 nm. Output laser power was 100 mW, and measurements were performed using an Olympus lens of $100\times$ to focus the laser beam onto an area that was 1 μm in diameter. Analyses were carried out on 30 μm polished thin sections. Spectra result from the average of five acquisitions of 10–20 s for each point measured to optimize the signal/noise ratio. Raman spectra were recorded in two spectral intervals: 200–1250 cm^{-1} for structural bonding characterization and 3550–3800 cm^{-1} for the characterization of hydroxyl groups. Serpentine species were mainly identified by comparing spectra with those already published (Auzende et al. 2004; Lemaire 2000), focusing on the OH stretching range.

Mineral chemistry

Electron microprobe analyses of minerals were carried out with a Cameca SX 100 at Service Commun de Microscopie Électronique et de Microanalyses (SCMEM, Nancy, France). All analyses of major elements, Na, Mg, Al, Si, K, Ca, Ti, Cr, Mn, Fe, Ni, were made against natural and synthetic mineral standard: albite (Si, Na), corundum (Al), andradite (Ca), olivine (Mg), hematite (Fe), MnTiO$_3$ (Mn, Ti), NiO (Ni), orthoclase (K), with the exception for serpentine measurements for which Mg was calibrated using natural clinochlore. Acceleration voltage and beam current were 15 kV and 12 nA, respectively, the counting time was 10 s, and standard correction procedures were applied. The beam diameter was focused to 1 μm. Total Fe content is calculated on a divalent basis, as FeO. Structural formulae were calculated based on of the following number of oxygens: olivine, 4; pyroxene, 6; lizardite, chrysotile and polygonal serpentine, 7. Antigorite has a general formulae $Mg_{3m-3}Si_{2m}O_{5m}(OH)_{4m-6}$ that differs from the idealized serpentine formula $Mg_3SiO_5(OH)_4$ by a minor $Mg(OH)_2$ depletion, m being the number of tetrahedra along an entire wavelength. Structural formulae for antigorite were calculated based on $m = 17$.

Fe^{2+} and Fe^{3+} contents in serpentine were calculated using the approach described by Beard and Frost (2017). Thus, in the $(Mg + Fe_T)$ pfu vs. $(Si + Al)$ pfu space, the microprobe analyses of serpentine lie along a linear trend that extends from pure Mg serpentine (lizardite/chrysotile or antigorite) to brucite $(Mg(OH)_2)$. The trend towards brucite is a consequence of extremely fine-grained serpentine–brucite intergrowths. According to Beard and Frost (2017), the deviation of a serpentine analysis from the brucite trend reflects the stoichiometric effects of ferric iron substitutions in the crystal chemistry of serpentine. Here, a

full dioctahedral substitution is assumed, meaning that ferric iron is accommodated in the serpentine structure by substitution for divalent cation plus the addition of a vacancy in the octahedral sheet. In this case, a serpentine that integrates a significant amount of ferric iron would deviate from the brucite trend, showing lower $(Mg + Fe_T)$ pfu at a given $(Si + Al)$ pfu. Considering that this deviation is only caused by ferric iron substitution, the following equation provides Fe^{3+} pfu:

$$Fe^{3+} = -x \times (Si + Al) + 7 - (Mg + Fe_T), \qquad (1)$$

where x is the ideal number of Si cations when the serpentine formula is calculated for seven oxygens (i.e., 2 in lizardite/chrysotile and 2.05 in antigorite).

A High-Resolution Laser Ablation Inductively Coupled-Plasma Mass Spectrometer (HR-LA-ICP-MS) at the Geosciences Ocean laboratory (Brest, France) composed of a 193 nm MicroLas CopexPro Coherent coupled with an Element II ICP-MS has been used for trace element analyzes. Laser ablations were performed with a constant 5 Hz pulse rate, with an ablation crater of 90–120 μm in diameter. The number of pulses was 200, which is sufficient to form a long and stable signal for integration. The ablated material is transported using a constant He flow and mixed with Ar in a cyclone coaxial mixer before entering the ICP torch and being ionized. The ions are then sampled, accelerated and focused before being separated and analyzed in the mass spectrometer. ^{29}Si content—known from prior electron microprobe analyses—was used as internal standard and concentrations were calibrated against the NIST 612 rhyolitic glass using reference values from Pearce et al. (1997). Data reduction was carried out using SILLS software, following the standard methods of Longerich et al. (1996). Detection limits were between < 1 and 60 ppb for most trace elements, < 0.5 ppm for B, Li, Mn, Co, Ni, As and between 1 and 50 ppm for Mg, Ca, Ti considering a spot size of 120 μm.

Stable isotope measurements

Stable oxygen and hydrogen isotope compositions were measured from separated serpentine fragments at the Stable Isotope Laboratory at the University of Lausanne. Separated powders were obtained by micro-drilling using a drill of 500 μm of diameter for the largest veins of antigorite and chrysotile. A smaller drill of 100 μm of diameter was used to sample the mesh core of lizardite. Serpentine samples were then purified from magnetite grains using a hand-held magnet and potential denser primary minerals were separated by settling in water. Oxygen isotopes were measured according to a method adapted after Sharp (1992). Between 1 and 2 mg of powder are loaded in a Pt sample holder and heated with a CO$_2$-laser under a F atmosphere and a pressure of 50 mbar.

The liberated oxygen is analyzed as O on a Finnigan MAT 253 mass spectrometer. Hydrogen isotope were measured by applying the method of Sharp et al. (2001). Between 0.5 and 1 mg of sample powder is loaded in a tin capsule and reduced by reaction with glassy carbon at 1450 °C in a helium carrier gas-producing H and CO. Produced gases are separated in a gas chromatograph and analyzed in a Finnigan MAT Delta Plus XL mass spectrometer configured to make hydrogen isotope analyses in continuous flow mode. Results are given in the standard δ-notation, expressed relative to V_{SMOW} in permil (‰). Replicate oxygen isotope analyses of the standards (UWG-2 garnet) yielded an average precision of $\pm 0.25‰$ for $\delta^{18}O$ values. The precision of the G1 biotite in-house standards for hydrogen isotope analyses was $\pm 2‰$.

Results

Serpentine petrography

In agreement with the work of Orloff (1968), whereas the degree of serpentinization is moderate to high throughout the ophiolite (> 50%, "facies normal", Fig. 2a, b), it is close to 100% near the base, giving to the rock a typical dark color ("facies de base"; Fig. 2c). Locally, near the top of the massifs, the degree of serpentinization is less than 10% ("facies superieur"). There, serpentine occurs along fracture walls and also forms mm-thick black veins pervasively surrounding preserved grains of olivine and pyroxene.

The base of the ophiolite consists of a schistose and intensely brecciated serpentinite sole of 20–300 m thick. Breccias are composed by mm to dm-scale blocks (phacoids) of totally serpentinized peridotite embedded in a matrix of sheared serpentinite. Several generations of serpentine can be identified even at naked eye: massive serpentinite is crosscut by mm to cm-thick, yellow to light-green serpentine veins (Fig. 2d). These veins are systematically surrounded by dark seams of magnetite and the overall is frequently crosscut by mm-thick fibrous veins, the latter being occasionally replaced by veins of greenish to white serpentine (Fig. 2e, f). This greenish to white serpentine may also compose large amounts of the breccia matrix. In thin section, the latest generations of serpentine occur almost exclusively as limited domains or veins formed after microfracture infilling (Fig. 3b–d). Larger domains of replacement can be found, but they usually correspond to the strongly deformed area where secondary serpentine composes the breccia matrix.

In the less serpentinized samples, serpentinization starts at the boundaries of olivine grains and along micro-fractures (Fig. 3). It progressively extends from the rim to the core of the grains as the serpentinization degree increases, giving the rock a typical mesh texture (see S1 in Fig. 3a). In general, olivine is strongly affected by serpentinization, while orthopyroxene remains relatively preserved or develop bastite rims around fresh cores. Iron released during serpentinization crystallized as magnetite rimming olivine grains and along mm-scale fractures, forming dark seams (Fig. 3a).

Fig. 2 **a, b.** Slightly (< 20%) to moderately (~ 50%) serpentinized peridotite, respectively, corresponding to the "facies supérieur" (**b**) and "facies intermediaire" (**a**) described in Orloff (1968). **c** Serpentinite from the base of the ophiolite nappe, just above the serpentinite sole. **d–f** Serpentinite from the serpentinite sole showing multiple generations of serpentine in the form of veins and fracture infilling. These serpentines include centimeter-scale greenish veins (**d**) that are crosscut by millimeter-scale veins filled by fibrous serpentine and/or light green to white-colored massive serpentine (**e, f**)
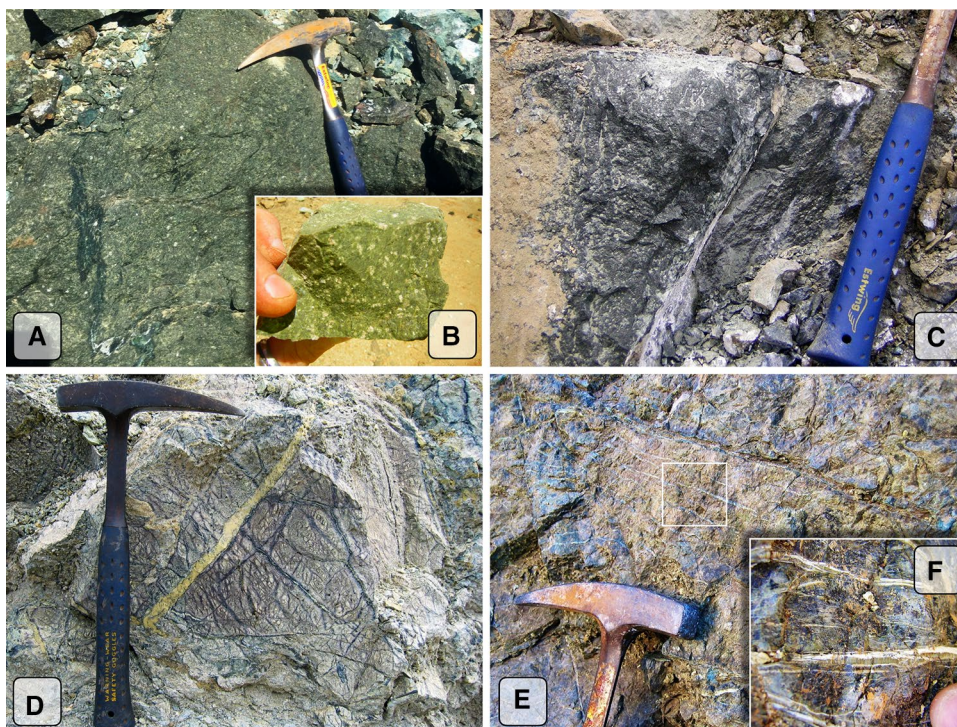
Fig. 3 **a** Microphotography (cross-polarized) of the typical mesh texture (S1) observed in serpentinized peridotite and serpentinites from the upper parts of the Peridotite Nappe. Black veins correspond to magnetite (sample MS60). **b** Microphotography (cross-polarized) of the serpentinite sole showing the primary mesh texture (S1) crosscut by 4 successive generations of serpentine veins (S2–S5; sample xx3786). **c** Microphotography (cross-polarized) of the serpentinite sole showing the primary mesh texture (S1) crosscut by S3 veins, itself crosscut by fiber-habitus S5 veins and the close association between S5 and S6 serpentines (sample xx3758). **d** Schematic representation of (**b**). *mgt* magnetite, *chr* chromite
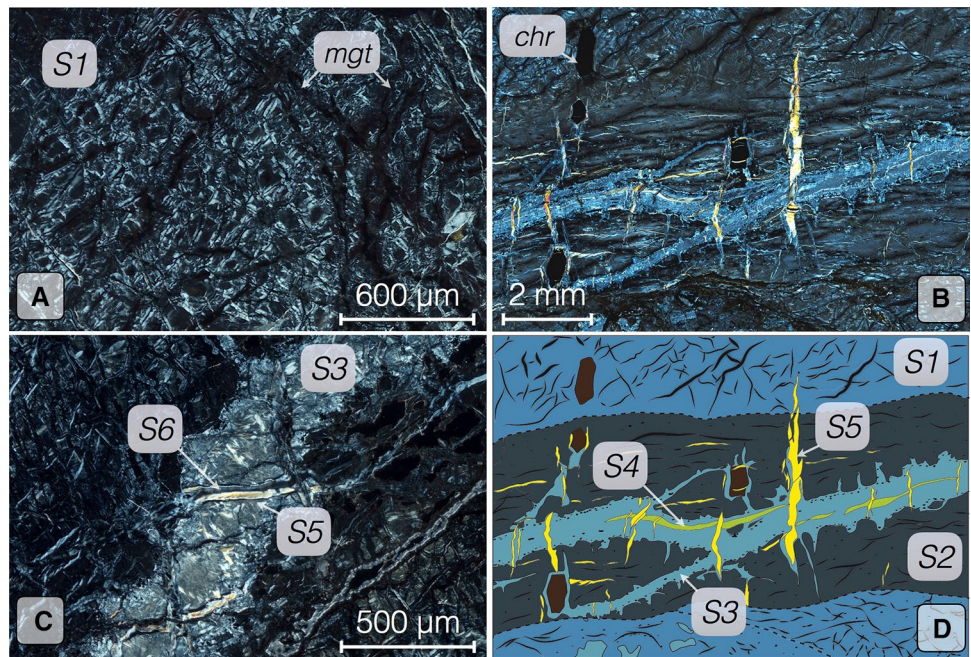
Six generations of serpentine have been identified in the sole (S1–S6 in Fig. 3). The first generation of serpentine after the primary mesh texture (S1) forms homogeneous domains that display the same grey color as the mesh texture under cross-polarized light (S2, Fig. 3b, d). Black veins of magnetite identical to those observed in the mesh texture are present in S2, and extend parallel to the S2 borders. The limits of the S2 domain are diffuse, suggesting progressive replacements of the mesh texture S1. Both serpentine generations are closely associated with μm to mm-thick veins of serpentine of a characteristic bluish-grey color under cross-polarized light (S3, Fig. 3b–d). S3 veins are made of decussate blades of tens of micrometers in size, giving these veins a typical interlocking texture. The borders of S3 veins are marked by the accumulation of magnetite grains, both inside and outside the veins. S4 veins occasionally crystallize in tension gashes, similarly to S5 veins and exhibit transitional texture between the decussate blades of S3 and the fibrous habitus that characterizes S5. Fibers can reach ~ 200 μm in size and have a grey to yellow birefringence under cross-polarized light (Fig. 3b, c). They are commonly oriented perpendicularly to the vein edges. The latest serpentine generation (S6) occurs as replacement of previous serpentine generations, forming veins (Fig. 3c) or covering large domains that form the matrix of breccias as shown by Ulrich et al. (2014) and Quesnel et al. (2016b).

Nature of serpentine polymorphs

The typical Raman spectra for the different generations of serpentine (i.e., from S1 to S6, as previously described) are displayed in Fig. 4. Their specific spectral signatures allow identifying serpentine species (Fig. 4; Auzende et al. 2004; Lemaire 2000). Except for minor changes in the low wavenumber region, the discrimination and identification of serpentine minerals are mainly based on the OH stretching bands located in the range 3600–3750 cm^{-1}. Lizardite characterized by peaks at 3685 and 3706 cm^{-1}, is the most abundant variety, forming the S1 and S2 generations. In contrast, the typical Raman spectrum obtained for S3 veins corresponds to antigorite, with characteristic peaks at 3670 and 3699 cm^{-1}. S5 perfectly matches with the spectral signature of chrysotile, and S4 corresponds to a mixture of antigorite (S3) and chrysotile (S5). Finally, the serpentine S6 is identified as polygonal serpentine, characterized by a weak band at 3648 cm^{-1} and a doublet at 3690 and 3697 cm^{-1} (Cathelineau et al. 2016).

Chemistry of primary minerals

The representative compositions in major and trace elements of primary minerals and each serpentine variety identified are presented in Tables 1 and 2. The supplementary table S1 provides all the data. Standard deviations are 2σ. Analyses of the primary minerals are consistent with those previously published for the NC peridotites (Frost et al. 2013; Mothersole et al. 2017; Pirard et al. 2013). Olivine is Fo$_{91}$ (Fig. 5) and has a NiO content of ~ 0.4 wt% (Ni = 0.1 pfu) and MnO content of ~ 0.16 wt%. Olivine is also characterized by an extreme depletion in trace elements so that they are usually close, or below, the detection limit. High-field strength elements (HFSE) have Primitive Mantle (PM)-normalized
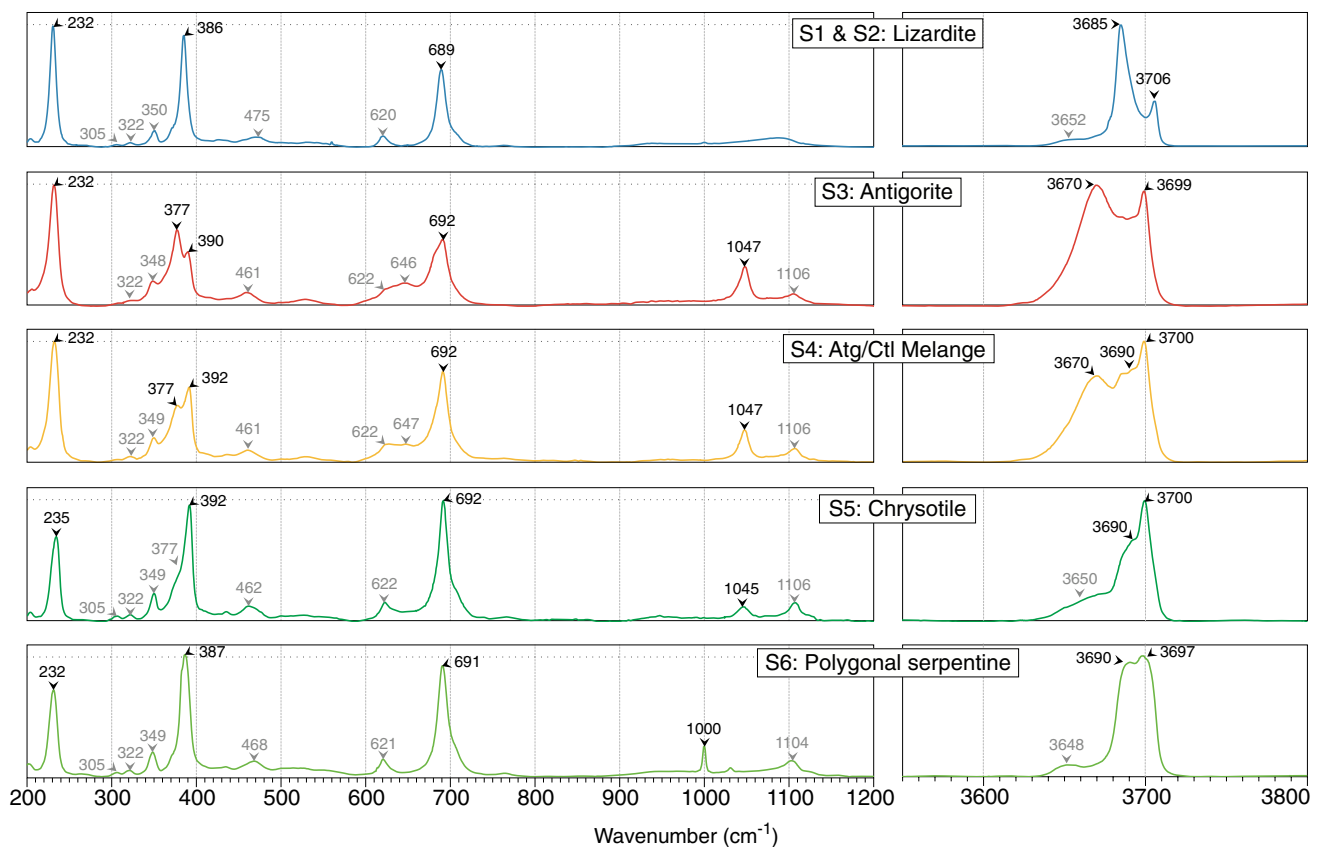
Fig. 4 Raman spectra of the main serpentine species identified in this study

concentrations varying between 10^{-3} and 10^{-1} (Fig. 6). Orthopyroxene is mainly enstatite and has a constant Mg# similar to olivine (0.91). CaO content ranges between 0.42 and 2.79 wt% with an average value of 1.06 wt% (Ca = 0.04 pfu). Al_2O_3 and Cr_2O_3 have concentrations ranging between 2.27 and 4.51 wt% and 0.56 and 0.88 wt%, respectively, and a corresponding Cr# of ~0.12 and down to 0.09, reflecting a high degree of depletion of the peridotite. PM-normalized trace element patterns show that orthopyroxene is strongly depleted in light rare-earth elements (LREE), with Ce_N/ $Yb_N < 0.05$. Clinopyroxene is diopside and is mainly present in spinel and plagioclase lherzolite, although some occurrences may be observed in harzburgite, mostly from exsolution in orthopyroxene. Clinopyroxene is characterized by slightly higher Mg# (~0.93) and Al_2O_3 of ~4.16 wt% (Al = 0.2 pfu) and Cr_2O_3 of 0.94 wt% (Cr# ~0.13). PM-normalized trace element patterns show a strong fractionation of LREE relative to heavy (H)REE (Ce_N/$Yb_N < 0.01$) and a nearly flat HREE pattern (Dy_N/Yb_N ~0.8). Slight Sr and Eu anomalies are observed and reflect equilibrium with plagioclase.

Chemistry of serpentine

Lizardite replacing primary minerals in the upper parts of the massif (upper serpentines) has been divided in four types: lizardite after olivine (i.e., in the mesh core), lizardite in the mesh rim, lizardite after orthopyroxene and lizardite after clinopyroxene. All have H_2O content of ~13 wt%, which is consistent with the hydroxyl stoichiometry of lizardite. Lizardite after olivine shows rather homogeneous compositions with ~41 wt% SiO_2 and MgO (Si = 2.0 pfu, Mg = 2.9 pfu) and ~4 wt% FeO (Fe^{2+} = 0.2 pfu). Compared to olivine, mesh cores have higher Al_2O_3 content (~0.3 wt%) and lower NiO content (~0.2 wt%). Mesh rims are characterized by lower SiO_2 and MgO contents (38 wt% and 37 wt%, respectively). FeO content is higher (> 10 wt%, Fe^{2+} = 0.5 pfu) and may reflect the presence of minute grains of magnetite in the mesh rims. Bastite contains 38–42 wt% SiO_2, and is usually characterized by lower Si at a given Mg + Fe_T compared to lizardite after olivine, and displays higher Cr and Al contents. Mg# varies between 0.91 and 0.97, with an average of 0.92 (Fig. 5). Bastites formed either after orthopyroxene or clinopyroxene do not show any difference in the major element concentrations. Regarding the Fe oxidation state

Table 1 Representative major element concentrations of primary minerals (olivine, orthopyroxene and clinopyroxene) and serpentines from NC peridotites

Structural position	Upper part of the ophiolite												Serpentinite sole							
Sample id	MS60-1	Ti-6-3	Ti-50A-07-6	Ti-50A-07-9	Ti-6-1	Ti-50A-07-3	Ti-50-2	Ti-48	Poum17	Ti-48	Ti-48-06	Poum-13	xx3786A-7	KOP-13	xx3786A-13	KOP3-5	xx3758-7	xx3786B-2	KOP3-3	KOP3-4
Type	Lizardite	Lizardite	Lizardite	Lizardite	Lizardite	Lizardite	Olivine	Olivine	Orthopyroxene	Orthopyroxene	Clinopyroxene	Clinopyroxene	Lizardite	Lizardite	Antigorite	Antigorite	Chrysotile	Chrysotile	Polygonal	Polygonal
Texture	Mesh core	Mesh core	Mesh rim	Mesh rim	Bastite	Bastite							Clast and breccia matrix	Clast and breccia matrix	Vein	Vein	Vein	Vein	Vein and breccia matrix	Vein and breccia matrix
Primary minerals	Olivine	Olivine	Olivine	Olivine	Opx	Cpx														
SiO_2	40.0	41.7	38.9	38.5	42.4	39.4	41.0	40.8	55.2	55.1	51.9	51.7	43.2	44.0	43.5	44.4	44.1	43.5	44.6	45.5
TiO_2	–	–	–	0.01	0.07	0.04	–	–	0.09	0.11	0.30	0.27	0.04	0.01	–	–	0.02	–	–	–
Al_2O_3	–	0.57	0.01	–	2.07	1.15	–	–	4.20	3.56	4.77	4.26	0.04	0.05	0.02	0.01	0.06	0.05	0.05	0.01
FeO	5.58	2.75	10.97	11.41	2.86	5.88	8.75	8.83	6.01	5.88	2.44	2.07	2.21	1.42	2.85	2.42	2.01	2.08	1.46	1.54
MnO	0.02	–	0.19	0.04	0.15	0.18	0.16	0.14	0.16	0.15	0.10	0.12	0.08	0.05	0.01	0.03	0.06	0.02	0.02	–
MgO	41.3	42.4	36.7	37.5	38.7	40.3	50.0	49.8	33.5	33.1	16.3	16.3	41.4	42.6	39.9	41.4	40.0	40.4	41.5	40.7
CaO	–	–	–	–	0.11	–	0.04	0.02	0.47	1.06	23.11	23.01	–	0.07	–	0.09	0.11	0.08	0.04	–
Na_2O	0.01	0.02	–	–	0.03	–	–	–	0.01	–	0.29	0.38	–	0.03	0.06	0.01	0.02	0.05	0.02	0.02
K_2O	–	–	–	–	0.01	–	–	–	–	–	–	–	0.02	0.01	–	–	0.02	0.01	–	0.02
Cr_2O_3	–	–	–	–	0.95	–	0.01	0.01	0.66	0.88	1.01	1.11	–	–	–	0.01	–	0.10	–	0.08
NiO	0.38	0.11	0.49	0.47	0.15	0.40	0.41	0.38	0.10	0.10	0.05	0.05	0.48	0.29	0.23	0.10	0.05	0.12	0.21	0.21
Total	87.3	87.5	87.3	87.9	87.5	87.3	100.3	99.9	100.4	99.9	100.2	99.3	87.4	88.5	86.6	88.4	86.4	86.4	87.9	88.1
Number of oxygen	7	7	7	7	7	7	4		6		6		7		6.823		7		7	
p.f.u																				
Si	1.92	1.95	1.91	1.88	1.97	1.86	1.00	1.00	1.90	1.91	1.88	1.89	2.00	2.01	1.98	1.98	2.06	2.04	1.99	2.02
Ti	–	–	–	–	0.002	0.002	–	–	0.002	0.003	0.008	0.007	0.001	–	–	–	0.001	–	–	–
Al	0.018	0.031	0.001	–	0.114	0.064	–	–	0.170	0.146	0.203	0.183	0.002	0.003	0.001	0.001	0.003	0.003	0.003	0.001
Fe^{3+}	–	–	0.027	0.021	0.020	–	–	–	–	–	–	–	0.023	0.017	0.027	0.026	0.011	0.016	0.054	0.057
Fe^{2+}	0.212	0.107	0.424	0.446	0.092	0.313	0.178	0.181	0.173	0.170	0.074	0.063	0.062	0.037	0.082	0.065	0.067	0.065	0	0
Mn	0.002	–	0.008	0.002	0.006	0.007	–	–	0.005	0.005	0.003	0.004	0.003	0.002	0.000	0.001	0.002	0.001	0.001	–
Mg	2.90	2.95	2.69	2.73	2.68	2.84	1.81	1.81	1.72	1.71	0.88	0.89	2.86	2.90	2.72	2.75	2.78	2.82	2.75	2.69
Ca	–	–	–	–	0.006	–	<0.001	<0.001	0.017	0.039	0.897	0.900	–	0.003	–	0.004	0.006	0.004	0.002	–
Na	0.002	0.002	–	–	0.002	–	–	–	<0.001	–	0.020	0.027	–	0.003	0.005	0.001	0.002	0.005	0.002	0.002
K	–	–	–	–	0.001	–	–	–	–	–	–	–	0.001	0.001	–	–	0.001	0.001	–	0.001
Cr	–	–	–	–	0.035	0.015	<0.001	0.007	0.018	0.024	0.029	0.032	–	–	–	<0.001	–	0.004	–	0.003
Ni	0.008	0.004	0.019	0.018	0.006	0.006	0.008	0.007	0.003	0.003	0.001	0.001	0.018	0.011	0.008	0.004	0.002	0.005	0.008	0.007
Mg#	0.93	0.96	0.86	0.86	0.97	0.90	0.91	0.91	0.91	0.91	0.92	0.93	0.98	0.99	0.97	0.98	0.98	0.98	1.00	1.00
$Fe^{3+}/(Fe^{2+} + Fe^{3+})$	–	–	0.06	0.04	0.18	–	–	–	–	–	–	–	0.27	0.31	0.25	0.28	0.14	0.20	1.00	1.00

Table 2 Representative trace element concentrations of primary minerals (olivine, orthopyroxene and clinopyroxene) and serpentines from NC peridotites

Sample name	Ti-6	Ti-50	Ti-6	Ti-50	Ti-50Ti-50	Poum-13	Ti-48	Poum-11	Ti-50	Poum-11	xx-3786a	Ti-47	xx-3758	KOP-3	Ti-47	xx-3758	xx-3786a	xx-3758	KOP-3	xx3786a
Structural position	Upper serpentinite										Serpentinite sole									
Type	Lizardite	Lizardite	Lizardite	Lizardite	Olivine	Olivine	Orthopyroxene	Orthopyroxene	Clinopyroxene	Clinopyroxene	Lizardite	Lizardite	Lizardite	Antigorite	Antigorite	Antigorite	Chrysotile	Chrysotile	Polygonal	Polygonal
Texture	Mesh core	Mesh core	Bastite	Bastite							Clast and breccia matrix	Clast and breccia matrix	Clast and breccia matrix	Vein	Vein	Vein	Vein	Vein	Vein and breccia matrix	Vein and breccia matrix
Primary minerals	Olivine	Olivine	Opx	Cpx																
Li	<0.071	<0.561	<0.088	<0.684	n.d	n.d	n.d	n.d	n.d	n.d	<0.088	<0.215	0.170749	<0.069	<0.209	0.352	<0.048	0.165	<0.173	<0.072
B	5.72	9.89	24.3	13.6	n.d	n.d	n.d	n.d	n.d	n.d	3.79	5.98	5.12	7.00	8.07	4.85	3.01	4.65	7.20	6.28
Ti	60.1	60.3	159	2163	14.0	14.0	646	239	1766	542	<1.80	b.d.l	2.71	<1.81	12.7	1.95	<1.64	<1.60	<4.56	7.36
Mn	166.712	847	635	1460	1057	1004	1090	1096	747	638	80.8	116	84.5	206	289	119	168	158	139	267
Co	31.8628	81.1	27.3	67.4	147	146	63.0	59.0	28.0	24.0	18.2	45.3	7.62289	22.8	85.2	19.9	9.59	14.3	48.1	33.2
Ni	783	4350	576	3068	3127	3179	806	725	415	415	1488	1424	905	908	2146	938	471	526	2756	904
As	<0.156	<2.19	<0.461	<1.85	n.d	n.d	n.d	n.d	n.d	n.d	<0.454	<1.23	<0.259	<0.366	<1.05	<0.209	<0.326	<0.180	<1.20	<0.316
Rb	<0.010	<0.062	<0.031	<0.113	<0.013	<0.014	<0.017	<0.015	0.054	0.085	0.045	0.120	0.051	0.029	0.164	0.053	0.044	0.125	0.057	0.025
Sr	<0.032	<0.218	0.131	<0.357	0.02	0.02	1.16	<0.015	0.39	0.92	0.545	1.334	1.454	0.416	2.245	2.847	0.384	2.306	0.556	0.308
Y	0.260	0.060	0.907	7.809	0.012	0.014	1.72	0.189	8.709	2.053	0.060	0.037	0.147	0.090	0.028	0.047	0.016	0.044	0.365	0.070
Zr	0.049	<0.084	0.030	0.729	0.025	<0.01	0.022	0.018	0.164	0.137	0.125	0.053	0.025	0.077	0.076	0.045	0.054	0.017	0.205	0.120
Nb	0.003	<0.021	<0.003	0.032	<0.005	<0.004	0.011	<0.006	0.015	<0.007	<0.002	<0.006	<0.002	<0.002	<0.015	<0.001	<0.001	<0.001	<0.009	<0.003
Sn	<0.0512	<0.318	<0.048	<0.526	n.d	n.d	n.d	n.d	n.d	n.d	<0.045	<0.212	<0.043	<0.070	<0.341	<0.047	<0.051	<0.034	<0.115	<0.037
Sb	0.007	<0.033	<0.008	<0.040	n.d	n.d	n.d	n.d	n.d	n.d	<0.009	<0.016	<0.005	0.048	<0.028	0.008	0.008	<0.005	0.021	0.010
Cs	<0.003	<0.035	<0.008	<0.049	<0.006	<0.009	<0.007	<0.013	<0.006	0.01	<0.008	<0.014	<0.005	<0.005	<0.019	0.012	0.007	0.018	<0.008	<0.007
Ba	0.008	<0.044	0.012	0.137	0.243	<0.018	0.283	0.055	0.864	0.248	0.131	0.406	0.211	0.151	0.405	0.339	0.163	0.370	0.098	0.066
La	0.004	<0.008	<0.002	0.126	0.006	<0.002	0.133	<0.003	0.041	0.032	0.018	<0.003	0.058	0.043	<0.008	0.020	0.005	0.014	0.110	0.017
Ce	0.004	<0.006	0.004	0.022	0.226	<0.001	0.195	<0.003	0.029	0.038	0.002	0.008	0.001	0.017	<0.010	0.003	0.007	0.008	<0.007	0.017
Pr	<0.0007	<0.003	<0.0007	0.124	0.003	<0.002	<0.003	<0.001	0.014	0.01	0.005	0.001	0.014	0.014	<0.003	0.004	<0.001	0.004	0.049	0.008
Nd	0.003	0.011	0.006	0.488	<0.017	<0.008	<0.013	<0.013	0.074	0.111	0.035	<0.007	0.057	0.082	<0.018	0.021	0.009	0.013	0.262	0.031
Sm	<0.012	<0.147	<0.014	1.028	<0.008	<0.037	0.015	<0.015	0.152	0.03	<0.017	<0.032	<0.008	<0.026	<0.038	<0.012	<0.007	<0.011	0.058	<0.009
Eu	<0.001	0.040	0.007	0.275	<0.003	<0.003	0.009	0.003	0.105	0.011	0.004	<0.005	0.002	0.007	<0.011	<0.002	<0.002	<0.001	0.021	<0.003
Gd	0.005	0.005	0.015	0.951	<0.013	<0.008	0.05	<0.008	0.684	0.116	0.001	<0.005	<0.0007	0.002	<0.002	0.001	<0.0008	0.001	0.008	0.001
Tb	0.020	<0.022	0.062		<0.001	<0.001	0.018	<0.002	0.186	0.026	0.014	<0.012	0.010	0.014	<0.025	<0.005	<0.005	0.007	0.065	0.013
Dy	0.035	<0.013	0.122		0.007	<0.005	0.2	0.023	1.307	0.282	0.007	<0.011	0.010	0.011	0.012	0.005	<0.004	0.006	0.024	0.007
Ho	0.010	<0.003	0.037		<0.003	<0.002	0.053	0.006	0.355	0.075	0.002	0.002	0.004	0.002	<0.002	0.001	<0.0007	0.001	0.009	0.002
Er	0.032	<0.014	0.118		<0.008	0.005	0.263	0.039	1.05	0.275	0.007	<0.011	0.012	0.006	<0.007	0.004	0.001	0.002	0.026	0.004
Yb	0.045	0.069	0.162	0.932	<0.027	<0.013	0.453	0.099	1.059	0.388	0.006	<0.015	0.011	0.006	<0.019	0.004	0.004	<0.008	<0.018	<0.008
Lu	0.007	0.006	0.027	0.155	0.002	0.003	0.072	0.017	0.144	0.056	0.001	<0.003	<0.001	<0.001	<0.003	0.001	<0.0003	<0.001	<0.005	0.002
Hf	0.005	0.019	0.005	0.062	<0.006	<0.003	<0.007	<0.003	0.052	0.008	0.003	0.006	<0.004	<0.005	0.007	0.003	0.002	0.002	<0.010	<0.003
Ta	0.001	<0.013	<0.005	<0.019	<0.003	<0.001	<0.001	<0.003	0.003	0.006	<0.003	<0.005	0.004	<0.005	<0.010	<0.003	<0.002	<0.003	<0.015	<0.002

Table 2 (continued)

Structural position	Upper serpentinite										Serpentinite sole									
Type	Lizardite		Lizardite	Lizardite	Olivine		Orthopyroxene		Clinopyroxene		Lizardite			Antigorite			Chrysotile	Polygonal		
Texture	Mesh core		Bastite	Bastite							Clast and breccia matrix			Vein			Vein	Vein and breccia matrix		
Primary minerals	Olivine		Opx	Cpx																
Sample name	Ti-6	Ti-50	Ti-6	Ti-50	TI-50	Poum-13	TI-48	Poum-11	Ti-50	Poum-11	xx-3786a	Ti-47	xx-3758	KOP-3	Ti-47	xx-3758	xx-3786a	xx-3758	KOP-3	xx-3786a
Pb	0.007	0.063	0.003	0.045	0.055	0.028	<0.026	0.039	0.732	0.158	0.019	0.014	0.071	0.025	0.027	0.025	0.027	0.024	0.069	0.003
Th	0.002	<0.007	<0.001	<0.005	0.006	<0.001	<0.002	<0.001	0.004	0.005	0.001	<0.0003	<0.002	<0.0008	<0.002	<0.002	0.001	<0.0008	<0.002	<0.0005
U	0.002	0.002	<0.0004	<0.004	<0.003	0.002	<0.004	<0.001	0.003	0.002	0.001	0.024	0.003	0.010	<0.003	0.016	0.008	0.043	0.014	0.003

in upper serpentines, our estimates show that Fe is mostly divalent ($Fe^{3+}/Fe_T < 0.1$, Fig. 5d), consistently with previous estimates made by Beard and Frost (2017).

Primitive Mantle normalized trace element patterns of upper serpentines are presented in Fig. 6. Despite some slight differences (particularly some enrichments in large ion lithophile elements, LILE), PM-normalized trace element patterns of serpentines match well those of primary minerals. Minor and trace elements in lizardite after olivine is highly depleted (Ti: 10.0–85.8 ppm; Mn: 125–1059 ppm; Co: 18.7–81.1 ppm; Y: 0.060–0.375 ppm), with a strong fractionation between LREE and HREE ($0.008 < (Ce/Yb)_N < 0.132$). Lizardite after orthopyroxene is slightly less depleted in minor and trace elements (Ti: 158–174 ppm; Mn: 568–635 ppm; Co: 26.8 ppm; Y: 0.907–0.994 ppm) but still shows LREE depleted patterns and strong LREE/HREE fractionation ($0.02 < (Ce/Yb)_N < 0.162$) similar to lizardite after olivine. LREE are depleted in serpentine after clinopyroxene. Elements such as Y (7.81 ppm), Ti (2163 ppm), Mn (1460 ppm) and Co (67.4 ppm) are enriched compared to lizardite after olivine and orthopyroxene. Only one occurrence of lizardite after clinopyroxene was found, confirming that the clinopyroxene is more frequently transformed into amphibole (tremolite) than serpentine during the hydration processes. Regarding fluid-mobile elements (FME), upper serpentines are enriched in B (4.71–24.3 ppm), Sb (0.007–0.016 ppm) and U (0.854–2.74 ppm) and depleted in Li and Sr with respect to Depleted Mantle (DM) values (Fig. 7). More specifically, Pb and Sr concentrations are similar to those previously published for NC serpentinized peridotites (Secchiari et al. 2016, 2019; Ulrich et al. 2010), and overlap the fields of abyssal serpentinites and subducted serpentinites with some sedimentary contributions. Upper serpentinites display B, Li and Sb concentrations lower than those of other serpentinites worldwide (Fig. 7). Arsenic is always below the detection limits.

In the serpentinite sole, all serpentine species display homogeneous major and trace element compositions. They contain ~ 44 wt% SiO_2 (Si = 2.0 pfu), ~ 40 wt% MgO (Mg = 2.8 pfu), ~ 13 wt% H_2O and they are characterized by very low FeO (~ 2 wt%, Fe ≤ 0.1 pfu) and Al_2O_3 (< 0.1 wt%, Al < 0.005 pfu; Fig. 5) and very high Mg# (~ 0.98) compared to upper serpentines. Calculated Fe^{3+}/Fe_T ratio shows that serpentines from the sole integrate significant amounts of ferric iron: on average, lizardite and chrysotile have Fe^{3+}/Fe_T ratio of ~ 0.2, antigorite, 0.35, and polygonal serpentine, 0.7 (up to 1). They also show HFSE depletion similar to that described in upper serpentines. However, they are slightly more depleted in HREE and significantly more enriched in LREE, except Ce which has a similar concentration to that of moderately serpentinized NC peridotites. Serpentines from the sole display a strong Ce negative anomaly (Ce/Ce* = 0.009–0.739, Fig. 7). They also display enriched
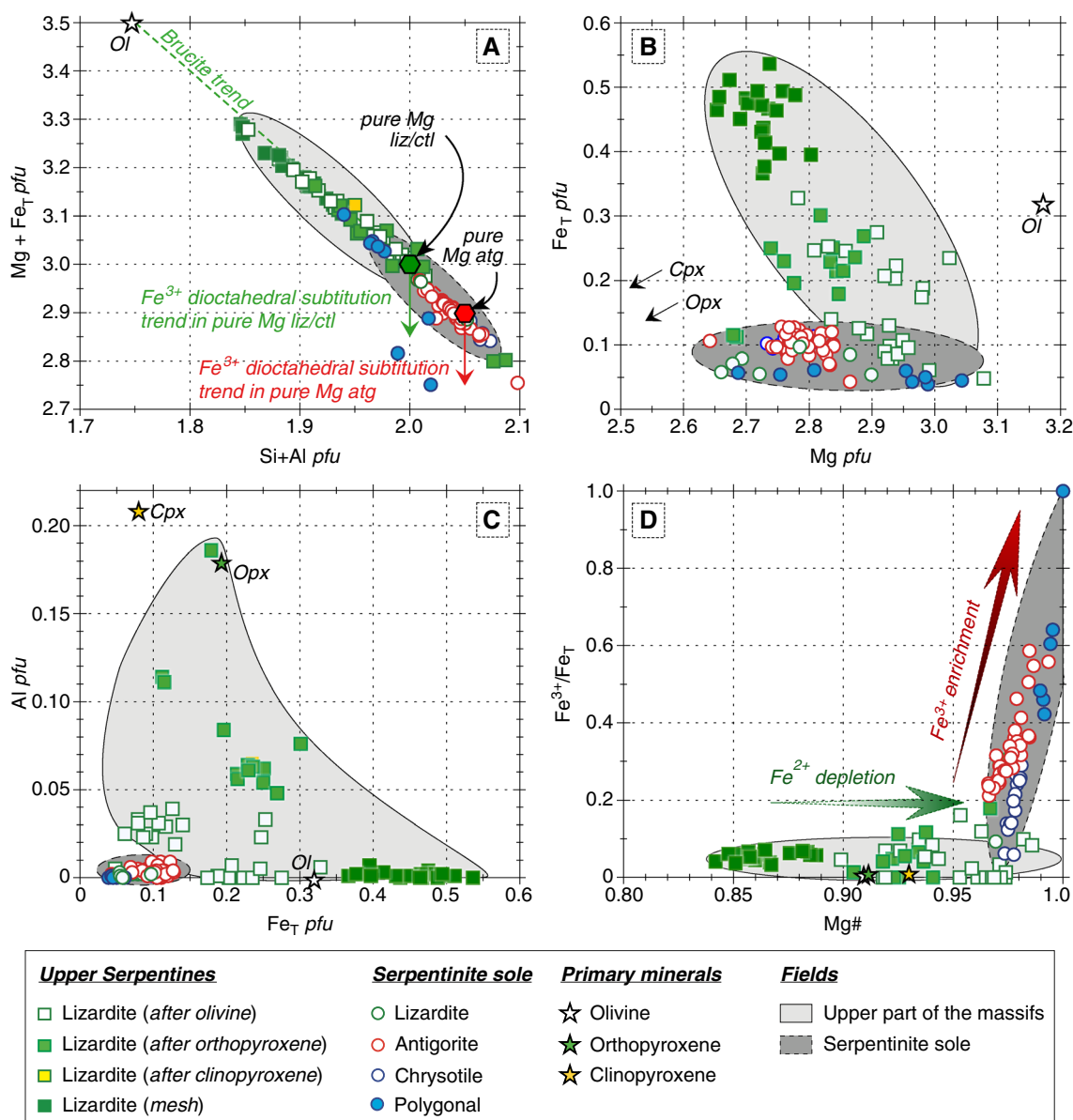
Fig. 5 Plots of **a** Si+Al cations vs. Mg+Fe_T cations; **b** Mg cations vs. Fe_T cations; **c** Fe_T cations vs. Al cations; and **d** Mg# ($Mg^{2+}/(Mg^{2+}+Fe^{2+})$) vs. Fe^{3+}/Fe_T (lower right), showing that serpentine from the sole integrates less Al and Fe_T and more oxidized iron than upper serpentines. Compositions of primary minerals are also shown. *Ol* olivine, *Opx* orthopyroxene, *Cpx* clinopyroxene. Atoms per for-mula units are calculated based on 7 oxygens for serpentine minerals, except for antigorite which is calculated based on 6.823 oxygens. Olivine and pyroxene structural formulas are calculated based on 4 and 6 oxygens, respectively, and then converted to 7 oxygens for comparison with serpentine minerals. Brucite and Fe^{3+} dioctahedral substitution trends are from Beard and Frost (2017)

concentrations in FME relative to upper serpentines (B: 2.13–8.52 ppm; Sb: 0.005–0.057 ppm; Li: 0.054–0.543; Cs: 0.004–0.022; Rb: 0.014–0.275 ppm; Ba: 0.066–0.952 ppm; Pb: 0.002–0.133; Sr: 0.202–4.05 ppm) with a pronounced U positive anomaly (U: 0.001–0.043 ppm; Fig. 6). Similarly to upper serpentines, as concentrations in the serpentinite sole were too low to be determined (Table 2).

O and H stable isotope composition

The $\delta^{18}O$ and δD values of fresh peridotites are +5.5‰ and −70‰, respectively, which are consistent with mantle rock compositions (Deloule et al. 1991; Eiler 2001). Serpentines display a wide range of $\delta^{18}O$ values from +1.7 to +13.9‰. In contrast, δD values are quite homogeneous (−107 to
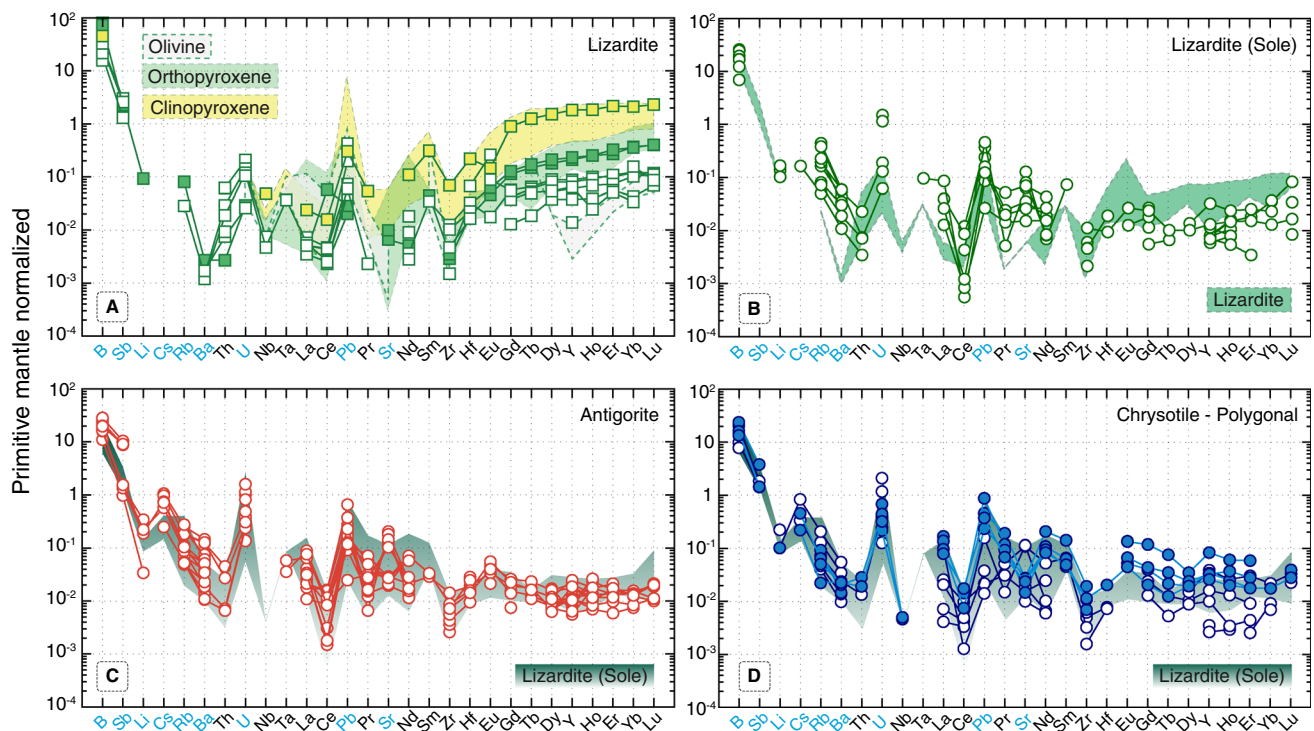
Fig. 6 PM-normalized extended trace element patterns of serpentine minerals. **a** Lizardite from upper serpentines compared to their magmatic mineral precursors (olivine, orthopyroxene, clinopyroxene). The first serpentine generation (lizardite S1) preserves the initial trace element patterns. **b** Trace element patterns of lizardite from the serpentinite sole (S2) compared to lizardite S1. **c** Trace element patterns of antigorite (S3) from the serpentinite sole compared to lizardite S2.

d Trace element patterns of chrysotile (S5) and polygonal serpentine (S6) from the serpentinite sole compared to lizardite S2. S1–S2 transition is marked by an enrichment in fluid-mobile elements (in blue), especially with a pronounced U positive anomaly and an enrichment in LREE except for Ce. S2 to S6 transitions occurred isochemically. Primitive-mantle values are from McDonough and Sun (1995)

−88‰). No systematic difference can be observed between serpentine species (Table 3).

The upper serpentines (i.e., lizardite) display a narrow range of isotopic compositions: $+5.4‰ < \delta^{18}O < +6.9‰$ and $-103‰ < \delta D < -97‰$. In the serpentinite sole, the $\delta^{18}O$ and δD values of lizardite are somewhat broader: $\delta^{18}O_{liz} = +2.2$ to $+5.7‰$ and $\delta D_{liz} = -107$ to $-97‰$. The whole range of values including other serpentine species from the sole is $+1.7$ to $+12.2‰$ for oxygen, -107 to $-88‰$ for hydrogen. Two samples (Ti 51a−1, −2, Poum 4–6, −2, −3) have traces of amorphous silica, and also the highest $\delta^{18}O$ values. Such high values are likely due to amorphous silica, which has high $\delta^{18}O$ values around $+30‰$ (Quesnel et al. 2016a). For this reason, these data will not be considered further in the following discussion. The isotopic compositions of serpentines are thus assumed to range between $+1.7$ and $+7.9‰$ for $\delta^{18}O$, and from -107 to $-88‰$ for δD.

Discussion

Deciphering the source of serpentinization fluids and conditions of serpentinization from the serpentine chemistry: a new modeling approach

The New Caledonia serpentines plot away from the field of oceanic serpentines defined in the literature (Sakai et al. 1990; Wenner and Taylor 1973), therefore excluding the involvement of seawater in the serpentinization process (Fig. 8a). Some trace element concentrations also confirm this inference (Fig. 7), since abyssal serpentines are usually characterized by a high U/Th ratio, attributed to seawater interaction with peridotite (Deschamps 2010; Frisby et al. 2016). U and Th are highly depleted in the mantle (e.g., Salters et al. 2002), but U is enriched in seawater relative to Th (Chen et al. 1986), leading to a significant fractionation
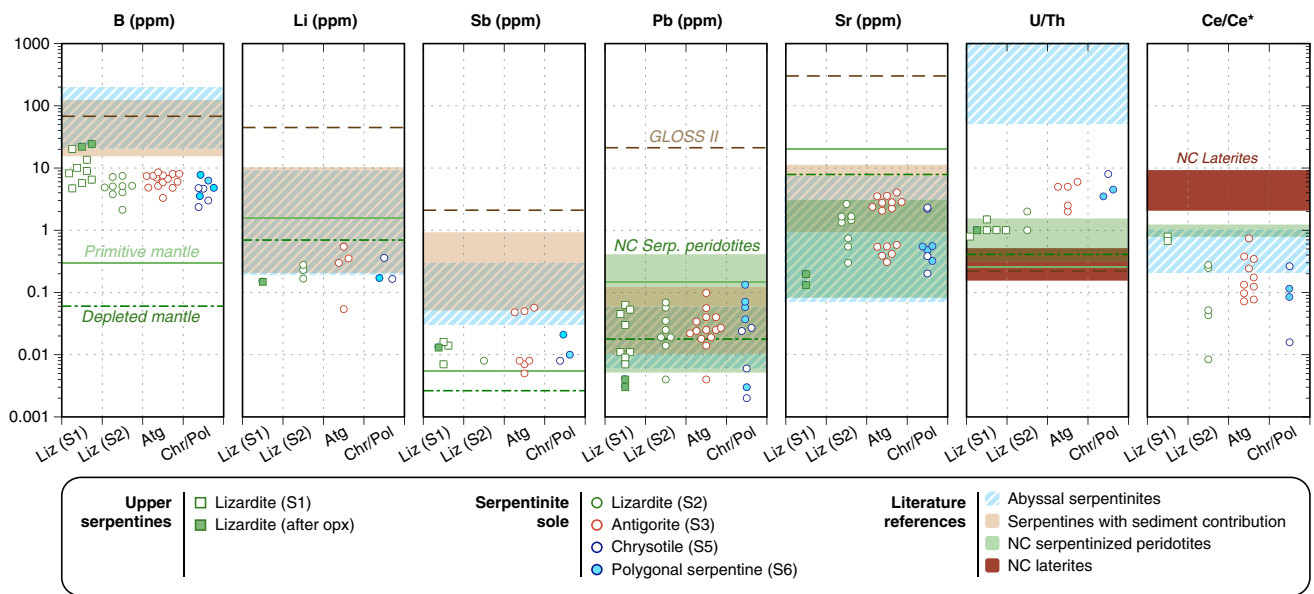
Fig. 7 Plots of concentrations of selected fluid-mobile elements (B, Li, Sb, Pb, and Sr), U/Th and Ce/Ce* ratios in serpentines from Upper serpentinites and from the serpentinite sole. Primitive and depleted mantle values are from McDonough and Sun (1995) and from Workman and Hart (2005), respectively, except for B, Li and Sb concentrations in the depleted mantle which are from Salters and Stracke (2004). Global subducted sediments (GLOSS II) concentra-

tions are from Plank (2014). Other concentration ranges are from Frisby et al. (2016) and Peters et al. (2017) for abyssal serpentinites; Lafay et al. (2013) and Peters et al. (2017) for serpentines with sedimentary imprints; Ulrich et al. (2010) and Secchiari et al. (2016, 2019) for NC serpentinized peridotites; Ulrich et al. (2019) for laterites. Ce/Ce* = $Ce_N/[(La_N*Pr_N)^{1/2}]$

between these elements when seawater is involved in serpentinization process. The Ce negative anomaly (Ce/Ce* < 1, with Ce/Ce* equals to $Ce_N/[(La_N*Pr_N)^{1/2}])$ is typical of the seawater where Ce^{3+} is oxidized tino the less soluble Ce^{4+} (Elderfield and Greaves 1982). Low Ce/Ce* is also a common feature in abyssal serpentines (Delacour et al. 2008; Frisby et al. 2016; Rouméjon et al. 2015). Frisby et al. (2016) have recently shown that seawater influences the LREE budget of serpentine through the addition of La and Pr, and that Ce/Ce* decreases in abyssal serpentines with increasing U/Th. NC serpentines, more specifically those from the serpentinite sole, are characterized by high U/Th and low Ce/Ce*ratios compared to moderately serpentinized NC peridotites (Fig. 7). However, U/Th ratio never exceeds 10 in our samples whereas it is >> 10 in abyssal serpentines (up to 10,000). Also, most of our samples display much larger Ce negative anomalies than that of abyssal serpentines, thus providing additional evidence that seawater was unlikely involved in the formation of NC serpentines.

Serpentine with δD values as low as − 100‰ have been identified in other places worldwide, forming the "Ophiolite serpentines" field defined by Wenner and Taylor (1973) where NC serpentines plot (Fig. 8a). These Ophiolite serpentines are commonly assumed to result from the interaction of peridotite with meteoric or metamorphic fluids either during obduction or during exhumation and retrograde re-equilibration of the peridotites (Früh-Green et al. 1996, 2001; Kyser

et al. 1999; O'Hanley 1996). Typically, very low δD values for serpentine minerals (< − 100‰) are attributed to late serpentinization events due to the circulation of meteoric waters under subsurface conditions. On the other hand, δD values in the range of − 100 to − 70‰ are better explained by the presence of composite fluids (Burkhard and O'Neil 1988; Früh-Green et al. 2001).

The O and H isotope compositions of a given serpentine depend on three main parameters: (1) the isotopic composition of the serpentinizing fluid ($\delta^{18}O_{fluid}$ and δD_{fluid}), (2) the serpentinization temperature (T), and (3) the water–rock ratio (W/R) during the reaction. The complex relationships between these three parameters on one hand, and the isotopic fractionation factors on the other hand, have been characterized experimentally and from the study of natural samples (e.g., Saccocia et al. 2009; Sakai and Tsutsumi 1978; Savin and Lee 1988; Wenner and Taylor 1973; Zheng 1993). The isotopic compositions of serpentinizing fluids may be calculated using calibrated serpentine–water isotopic fractionation factors, and assuming W/R values and temperature (e.g., Alt et al. 2012; Alt and Shanks Iii 2006; Früh-Green et al. 2001; Kyser et al. 1999; Rouméjon et al. 2015; Sakai et al. 1990; Thakurta et al. 2009). Alternatively, W/R can be determined if the composition of the serpentinizing fluid is known (Agrinier and Cannat 1997; Alt et al. 2007; Burkhard and O'Neil 1988; Magaritz and Taylor 1974; Rouméjon et al. 2015; Wenner and Taylor 1973). Conversely,

Table 3 Oxygen and hydrogen compositions of NC serpentines

Sample	Location	Protolith	Position	Type	$\delta^{18}O_{SMOW}$ (‰)	δD_{SMOW} (‰)
Por12-1	Massif du sud	Du	US	liz	2.2	− 106
Por12-2	Massif du sud	Du	US	liz	4.2	− 106
Por12-3	Massif du sud	Du	US	liz	2.9	− 106
Por6	Massif du sud	Hz	US	WR	5.3	− 66
Por11	Massif du sud	Hz	US	WR	5.5	− 75
Por12	Massif du sud	Du	US	WR	2.2	− 95
Kop6-1	Kopéto	Hz	Sole	liz	4.1	− 107
Kop6-2	Kopéto	Hz	Sole	ant	6.3	− 98
Kop6-3	Kopéto	Hz	Sole	ant	3.8	− 98
Kop6-4	Kopéto	Hz	Sole	ant	5.3	− 98
xx3758	Koniambo	Hz	Sole	ant	4.0	− 104
xx3773	Koniambo	Hz	Sole	ant	1.7	− 91
xx3778	Koniambo	Hz	Sole	ant	5.1	–
Ko-05–1	Koniambo	Hz	Sole	chrys	4.4	− 100
Ko-05–2	Koniambo	Hz	Sole	chrys	4.3	− 102
Ti 24–1	Tiébaghi	Lhz	Sole	liz	2.9	− 103
Ti 47–2	Tiébaghi	Lhz	Sole	liz	5.7	− 97
Ti 48.06–1	Tiébaghi	Lhz	US	liz	5.4	− 97
Ti 48.06–2	Tiébaghi	Lhz	US	liz	5.6	− 103
Ti 5–1	Tiébaghi	Hz	Sole	liz	2.4	− 95
Ti 51c-1	Tiébaghi	Lhz	Sole	liz	3.0	− 104
Ti 47–3	Tiébaghi	Lhz	Sole	ant	1.9	− 88
Ti 47–3 dup	Tiébaghi	Lhz	Sole	ant	2.1	− 88
Ti 52E	Tiébaghi	Lhz	Sole	ant	4.9	− 95
Ti 52E dup	Tiébaghi	Lhz	Sole	ant	5.3	− 95
Ti 5–3	Tiébaghi	Hz	Sole	chrys	1.7	–
Ti 51a-1	Tiébaghi	Lhz	Sole	chrys	9.5	− 91
Ti 51a-2	Tiébaghi	Lhz	Sole	chrys	10.8	− 91
Ti 54b	Tiébaghi	Lhz	Sole	chrys	4.9	− 94
Ti 51c	Tiébaghi	Lhz	Sole	WR	2.6	− 88
Ti 24	Tiébaghi	Lhz	Sole	WR	1.9	− 90
Ti 47	Tiébaghi	Lhz	Sole	WR	5.8	− 87
Ti 48.06	Tiébaghi	Lhz	US	WR	6.4	− 97
Poum 17-1	Poum	Lhz	US	liz	6.8	− 103
Poum 17-1 dup	Poum	Lhz	US	liz	6.9	− 103
Poum 18-1	Poum	Lhz	US	liz	6.5	− 101
Poum 4-5	Poum	Hz	Sole	liz	7.6	− 100
Poum 4-6	Poum	Hz	Sole	liz	13.9	− 94
Poum 4-1	Poum	Hz	Sole	ant	7.9	− 101
Poum 4-2	Poum	Hz	Sole	ant	12.2	− 104
Poum 4-3	Poum	Hz	Sole	ant	12.1	− 104
UWG-2 gnt (*n* = 16; valeur théorique: 5.8‰)					5.78 ± 0.25	–
G1 Biotite (*n* = 16; valeur théorique: − 66‰)					–	− 67 ± 2

US upper serpentinites, *Lhz* lherzolite, *Hz* harzburgite, *Du* dunite, *lz* lizardite, *atg* antigorite, *ctl* chrysotile, *pol* polygonal serpentine, *BR* bulk rock

the approximative temperature of serpentinization can be estimated using the serpentine-magnetite geothermometer, based on the oxygen isotope fractionation between these two cogenetic minerals (Wenner and Taylor 1971).

Actually, this approach is somewhat unsatisfactory because it requires knowing or arbitrarily setting at least one of the parameters listed above. For example, in the oceanic context, serpentine fluids are relatively well constrained because they

are either seawater or seawater modified by hydrothermal fluids (Agrinier and Cannat 1997). But for fluids derived from ancient lithospheric remnants, $\delta^{18}O_{fluid}$ and δD_{fluid} are generally unknown and need to be assumed or calculated. It follows that the serpentine-magnetite geothermometer can hardly be used in the case of multiple serpentinization events since the related generations of magnetite are challenging to identify and separate.

In this study, we developed a new approach based on Monte Carlo simulations to constrain the source of fluids in equilibrium with NC serpentines based on their oxygen and hydrogen isotope compositions. Figure 8b–d shows the result of one million Monte Carlo simulations using the isotopic fractionation factors of Wenner and Taylor (1973) (as modified by O'Hanley 1996) for oxygen isotopes:

$$1000 \ln \alpha_{serpentine-water}^{^{18}O-^{16}O} = 1.69 \times 10^6 / T^2 - 4.23, \tag{2}$$

and of Saccocia et al. (2009) for hydrogen isotopes:

$$1000 \ln \alpha_{serpentine-water}^{D-H} = 3.436 \times 10^6 / T^2 - 34.736 \times 10^3 / T + 21.67, \tag{3}$$

where T is the temperature in Kelvin. It should be noticed that the use of oxygen isotope fractionation factors from Saccocia et al. (2009) provides quite similar results to those of Wenner and Taylor (1971) in the temperature range of 250–450 °C. However the serpentine–water $^{18}O-^{16}O$ fractionation factor of Wenner and Taylor (1971) is applicable for a wide range of temperature, contrarily to the experimental approach of Saccocia et al. (2009) whose fractionation factor was calibrated for temperatures > 250 °C. As a consequence, the use of the Wenner and Taylor fractionation factor was found more consistent with calculating the $\delta^{18}O$ composition of serpentinizing fluids when no other constraint on serpentinization temperature is available.

The O and H isotope compositions of a serpentine can be calculated by applying Sheppard et al. (1969) mass-balance equation:

$$\delta_{serpentine} = \frac{\delta_{mantle} + W/R \times \left(\delta_{fluid} + 1000 \ln \alpha_{serpentine-water} \right)}{1 + W/R}, \tag{4}$$

with $\delta_{serpentine}$, δ_{mantle} and δ_{fluid} are the O and H isotope compositions of the serpentine, the mantle and the serpentinizing fluid, respectively, W/R is the fluid–rock ratio and $1000\ln\alpha$ is the fractionation factor calculated with Eqs. (2) and (3). Mantle values of $\delta^{18}O = +5.5‰$ and $\delta D = -80‰$ have been chosen for the composition of the starting material (Deloule et al. 1991; Eiler 2001). Other parameters are defined randomly for each simulation in the following ranges: $50 < T°C < 450$, $0.13 < WR < 1000$, $-40 < \delta^{18}O_{fluid} (‰) < 40$ and $-200 < \delta D_{fluid} (‰) < 20$ (see Fig. 8). Although serpentine can be stable at temperature up to ~ 700 °C, the

temperature of serpentinization rarely exceeds 350 °C at spreading centers and 400–500 °C in subduction zones (e.g., Evans 2004; Klein et al. 2013; Ulmer and Trommsdorff 1995). Low-temperature serpentinization remains poorly documented, even though some authors argued for serpentinization might occur at temperature lower than 80 °C (e.g., Agrinier et al. 1995; Bonatti et al. 1984). Thus, a low-temperature threshold of 50 °C was chosen arbitrarily. The range of fluid–rock ratios was chosen considering that 0.13 is the minimum ratio required to convert an olivine into a serpentine stoichiometrically, and $\delta_{serpentine}^{WR=1000} \approx \delta_{serpentine}^{WR=\infty}$. δ_{fluid} thresholds were chosen so that almost all compositions of terrestrial fluids were covered (Hoefs 2009). In our modeling approach, a simulation is considered to be valid when the modeled serpentine displays $\delta^{18}O$ and δD compositions that are in the range of NC serpentinites ($1.7‰ < \delta^{18}O < 7.9‰$; $-107‰ < \delta D < -88‰$). Results are provided in supplementary materials and are presented in Fig. 8:Fig. 8b reports the calculated $\delta^{18}O$ and δD compositions of fluids that are able to reproduce a serpentine that matches the O and H compositions of NC serpentines. Among 1 million random simulations, ~ 6500 were consistent with the O and H signatures of NC serpentines. Figure 8c, d show, respectively, the calculated $\delta^{18}O_{fluid}$ and δD_{fluid} as a function of the correspondent temperatures of serpentinization. Results of Monte-Carlo simulations show that fluids in equilibrium with NC serpentines extend between the meteoric water line and an area defined between +3 and +8‰ in $\delta^{18}O$ and −80‰ and −60‰ in δD in which most of the results plot (~ 40% of 6500 simulations, see the red, white cross-hatched area in Fig. 8b). Fluids that fall into this area have interacted with the mantle at temperatures between ~ 250 and 430 °C (the white cross-hatched areas in Fig. 8c, d), while interactions with fluids showing negative $\delta^{18}O$ and higher δD signatures ($> -60‰$) occurred at lower temperatures (100–200 °C; Fig. 8c, d). With a few exceptions, our calculations show that NC serpentines were formed at relatively high W/R (> 1) (see Figure S1 in supplementary materials).

Origin of NC serpentinites

From deep serpentinization…

Based on the new petrological, mineralogical, geochemical and modeling data presented here, the chronology of serpentinization of NC peridotites would be as follows. First, the decreasing serpentinization degree from bottom to the top of the Peridotite nappe is good evidence for a fluid circulation mainly located at the base of the ophiolite. Since the NC ophiolite was in the forearc position for ~ 20 Ma before its obduction on the Norfolk Ridge, the most likely source of the fluids forming pervasive lizardite S1 would come from

dehydration of the subducting slab. As our results fall into the Alpine Ophiolite-type field of Wenner and Taylor (1973), they are consistent with this assumption. Consequently, three potential sources of fluids present in the recycled oceanic lithosphere can contribute to hydrating the mantle wedge: the altered oceanic crust (AOC), the subducted sediments and the subducted abyssal serpentinites. The fluids in equilibrium with all of these components have distinct signatures in trace elements and stable isotopes that also sharply differ from the composition of the mantle wedge (Eiler et al. 1998; Kodolanyi et al. 2012; Peters et al. 2017). One of the best examples documented worldwide is provided by the formation of serpentine mud volcanoes along the Marianna Trench (Fryer 1992). The geodynamics in this region approximates the one assumed for the South Loyalty Basin at the subduction time, and the occurrence of serpentinite seamounts provide a unique window for studying fluid circulations into the forearc mantle. Alt and Shanks III (2006) used typical $\delta^{18}O$ and δD values for the AOC, oceanic sediments, and abyssal serpentinites to predict the isotopic compositions of fluids in equilibrium with each subducted component, and determine the source of serpentinizing fluids in the Marianna forearc mantle. In their modeling, they assumed that the metasomatized basaltic basement has $\delta^{18}O = +8$ to $+11‰$ and $\delta D = -90$ to $-120‰$ (Alt 2003), and used a simplified AOC mineralogy with 49% albite, 49% chlorite and 2% calcite. The dehydration of metabasalts having these isotopic compositions and mineralogy would produce, therefore, fluids with $\delta^{18}O$ values of $+2$ to $+8‰$ (up to $+10‰$ at 400 °C) and δD values of $-50‰$ to $-90‰$. Similarly, the authors calculated higher $\delta^{18}O$ ($+12$ to $+16‰$) and δD (-20 to $-40‰$) values for sediment-derived fluids and $\delta^{18}O$ and δD in the range of $+5$ to $+9‰$ and -5 to $-30‰$ respectively for serpentine-derived fluids at ~ 200–350 °C (Fig. 8b). By comparison, the main O and H isotope values calculated for fluids in equilibrium with NC serpentinites (the red, white cross-hatched area in Fig. 8b) are consistent with fluids coming from the dehydration of an AOC. On the contrary, neither sediment-derived fluids nor serpentine-derived fluids fit our modeled serpentinizing fluids. Our simulations also predict that AOC-derived fluids interacted with the forearc peridotites at temperatures of 250–430 °C (Fig. 8c, d). These temperatures are close to those of AOC dehydration usually proposed in forearc settings (200–450 °C; Alt and Shanks Iii 2006; Rüpke et al. 2004). Additionally, the maximum temperature of 430 °C estimated by our simulations may be lowered to ~ 350 °C based on field observations: lizardite is commonly replaced by antigorite at temperature > 350 °C in (supra)-subduction environments (Evans et al. 1976; Evans 2004; Ulmer and Trommsdorff 1995, 1999). This replacement has never been observed in the NC ophiolite, where lizardite is the dominant serpentine variety, while antigorite

is mainly restricted to synkinematic crack seals (Cluzel et al. 2019; Quesnel et al. 2016b).

Regarding trace elements, the evolution of the mantle wedge composition interacting with slab-derived fluids is evaluated by proposing a single-step process where the fluids that migrate from the descending slab are mixed with the overlying forearc mantle. Trace element concentrations of a slab-derived fluid C_f can be estimated by applying the following equation:

$$C_f = \frac{C_0 \times M}{F}, \tag{5}$$

where C_0 is the concentration of an element in the subducted component (i.e., the AOC, the sediments or the serpentinites), M is the mobility (in percent) of an element during the dehydration of a subducted component, and F is the weight fraction of fluid extracted from the subducted component (Sano et al. 2001). All parameters used for the modeling of trace elements, references and results of calculations are summarized in Table 4. The weight fraction of fluids released from the AOC and sediments is assumed to be 1.5 and 3 wt%, respectively, in agreement with estimates previously published (Peacock 1990; Rüpke et al. 2004). The lizardite–antigorite transition in the subducting slab could have released fluids at temperatures below 350 °C in the forearc subducted slab. Thus, pure Mg–lizardite contains 13 wt% H_2O, while pure Mg–antigorite ($m = 17$) only contains 12.3 wt% H_2O. Consequently, the weight fraction of serpentine-derived fluids was set to ~ 0.7 wt%. Data of element mobility during dehydration processes are taken from experimental studies on natural pelite for sediments (Aizawa et al. 1999), natural amphibolite for AOC (Kogiso et al. 1997; Sano et al. 2001) and natural antigorite for serpentinite (Tenthorey and Hermann 2004). U, Th, B and Zr are used because of their behavior during dehydration and their respective concentrations in the slab components: Th and Zr mobilities are rather low in hydrous fluids, while B is highly mobile. U mobility depends on its oxidation state: it is immobile in its reduced form U^{4+} while it is mobile in its oxidized form U^{6+} (Brenan et al. 1995). Actually, the high solubility of uranium in subduction zone fluids has been reported by several studies (e.g., Bailey and Ragnarsdottir 1994; Bali et al. 2010). All of these elements are enriched in sediments (Plank 2014) and depleted in the mantle (Salters and Stracke 2004; Secchiari et al. 2019). The U/Th ratio is low in sediments, but is roughly similar in AOC and abyssal serpentinites (Table 4). However, the U/Th ratio is more fractionated during serpentine dehydration than during AOC dehydration (Kogiso et al. 1997; Tenthorey and Hermann 2004). As a consequence, the U/Th ratio is higher in serpentine-derived fluids than in AOC fluids, and is the lowest in sediment-derived fluids (Fig. 9). Subducted serpentinites
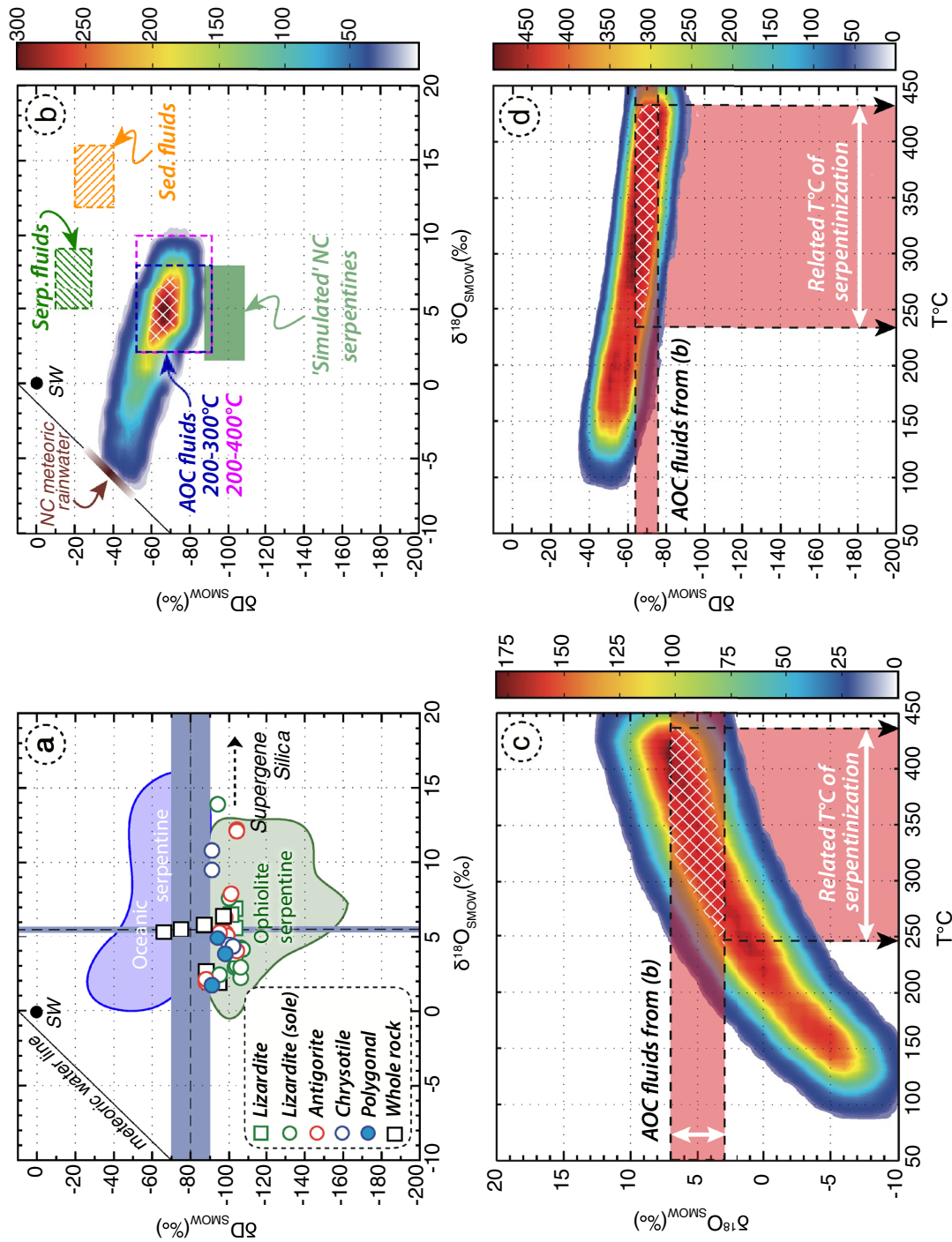
Fig. 8 **a** δD vs. δ¹⁸O of NC serpentines. Blue and green fields represent the isotopic compositions of oceanic serpentinites and ophiolite serpentinites, respectively, (Wenner and Taylor 1973; Früh-Green et al. 2001). The black arrow shows the trend formed by samples contaminated by supergene silica (δ¹⁸O > +29‰; Quesnel et al. 2016a, b). Grey areas indicate the range of mantle compositions in δ¹⁸O and δD, with average values of +5.5‰ and −80‰, respectively, (Deloule et al. 1991; Eiler 2001). **b** Calculated δ¹⁸O vs. δ¹⁸O compositions of serpentinizing fluids (represented as a density field) in equilibrium with NC serpentines, over 1,000,000 Monte-Carlo simulations, (~6500 positive results, i.e., consistent with the isotopic compositions of NC serpentines, over 200–400 °C, with subducted sediments (sed. fluids) and with subducted serpentines (serp. fluids) at 200–350 °C. The O and H compositions of fluids in equilibrium with the altered oceanic crust at 200–400 °C, see the main text for more details about the modeling). The O and H compositions of fluids in equilibrium with the altered oceanic crust at 200–400 °C, with subducted sediments (sed. fluids) and with subducted serpentines (serp. fluids) at 200–350 °C are calculated according to the modeling approach of Alt and Shanks III (2006). NC meteoric rainwater compositions are from Nicolini et al. (2016). **c**, **d** Calculated δ¹⁸O_fluid and δD_fluid vs. temperature of serpentinization. The white cross-hatched area indicates simulations that fall into the red area in **b** (~40% of >6500 simulations). Colorbar values correspond to the number of pixels in one grid cell of a size of +1‰ (δ¹⁸O) by +10‰ (δD) in **b**, 50 °C (T) by +1‰ (δ¹⁸O) in **c** and 50 °C (T) by +10‰ (δD) in **d**

Table 4 Chemical compositions, mobilities and references used for trace element modeling

Element	B	Th	U	Zr	U/Th	B/Zr	References
NC mantle wedge	0.06	0.001	0.0005	0.053	0.5	1.13	U, Th, Zr: Secchiari et al. (2016, 2019); B: Salters and Stracke (2004)
AOC	5.2	0.070	0.300	66.5	4.29	0.078	U, Th, Zr: Staudigel et al. (1996); B: Smith et al. (1995)
Mobility (%)	60	37.7	29.1	0.1			Kogiso (1997); Sano et al. (2001)
AOC-derived fluid ($F = 1.5\%$)	208	1.76	5.82	4.43	3.31	46.9	Weight fraction of fluid F: Peacock (1990); Rüpke et al. (2004)
GLOSS II	67.9	8.10	1.73	129	0.214	0.526	Plank (2014)
Mobility (%)	70	2.5	3.0	0.1			Aizawa et al. (1999)
Sed-derived fluid ($F = 3\%$)	1584	6.75	1.73	4.3	0.256	368	Weight fraction of fluid F: Peacock (1990); Rüpke et al. (2004)
Abyssal serpentines	50	0.073	0.569	2.4	7.79	20.8	Peters et al. (2017)
Mobility (%)	39.2	2	10	0.1			Tenthorey and Hermann (2004)
Serp-derived fluid ($F = 0.69\%$)	2841	0.212	8.25	0.348	39.0	8167	Weight fraction of fluid F: Water loss during Lz/Ctl to Atg transition

have a high B/Zr ratio (> 20), contrarily to subducted sediments and AOC, which are characterized by low (< 1) to very low (< 0.1) B/Zr ratios, respectively. Considering these ratios and the high mobility of B in fluids compared to Zr, the addition of subduction zone fluids in the mantle wedge leads to an increase of B/Zr ratio towards ~ 50 for AOC-derived fluids, ~ 370 for sediment-derived fluids and up to $\sim 8,200$ for serpentine-derived fluids. Consistently with the conclusions drawn from the stable isotope study, the trace element modeling suggests that NC upper serpentines were likely formed by the interaction with AOC-derived fluids, with nevertheless some addition of sediment-derived fluids ($< 30\%$, Fig. 9). This result is consistent with the highly radiogenic strontium isotope compositions of some NC serpentines from which a metasedimentary contribution was inferred (Cluzel et al. 2019). The modeling also indicates that the amount of slab-derived fluids that interacted with NC peridotites in the forearc was low, in the range of < 0.1–3 wt% (Fig. 9). The amount of sediment-derived fluids in the mantle wedge was consequently in the order of 0.9 wt% or less. Such a low amount of sediment-derived fluids is unresolvable by our modeling approach based on stable isotopes (Fig. 8). On the contrary, the Sr budget of sediments is high compared to the mantle so that a minute amount of sediments can buffer the Sr isotope system. These results together with the very low concentrations of As and Sb, which are proxies of the sedimentary contribution in serpentine chemistry (Deschamps et al. 2011, n2013; Hattori and Guillot 2007), imply that the amount of subducted sediments was low at the time of forearc peridotite hydration. The limited influence of sediment-derived fluids in the serpentine signature is also inferred by the lack of sedimentary prism, the latter being replaced by slices of basaltic rocks (i.e., the future Poya Terrane) scrapped off the down going plate during the Eocene NE-dipping subduction of the SLB (Cluzel et al. 2001, 2012b). In Fig. 9, the domain of

the serpentinite sole is more widespread than that of upper serpentines, with some samples plotting away from the modeling trends. This could reflect the effects of a later episode of fluids circulation (see the next section below) rather than those of slab-derived fluids contribution.

The subduction inception occurring at (or near to) the ridge axis in the SLB led to the development of a forearc magmatic activity from 55 to 47 Ma (Cluzel et al. 2006, 2016). During this period, thermal conditions in the forearc were high, causing the melting of the mantle wedge rather than its hydration. The continuous influx of fluids released from the dehydration of the oceanic crust of the subducting slab progressively cooled the forearc mantle, leading to the cessation of the forearc magmatism about 10 Ma after subduction inception (Cluzel et al. 2012a, 2016; Ulrich et al. 2010; Whattam et al. 2008). This period was long enough to alter significantly the oceanic crust exposed at the seafloor (Staudigel et al. 1981). Then, the AOC entering the subduction zone releases fluids in the overlying mantle wedge. Such fluids finally cause the massive serpentinization of the future NC ophiolite (Fig. 10a). It is worth noting that based on these results, no trace of oceanic serpentinization related to the opening of the SLB was identified so far. It is possible however that the serpentinized upper part of the upper plate (the Loyalty Basin) was removed early (i.e., soon after subduction inception) when the hot and buoyant lower plate had to force its way beneath the future Loyalty fore-arc. Such a feature could account for the absence of MORB-type basaltic crust on top of the peridotites in the Massif du Sud and the occurrence of fore-arc cumulates directly overlying highly depleted harzburgites and dunites.

…to (sub-) surface serpentinization

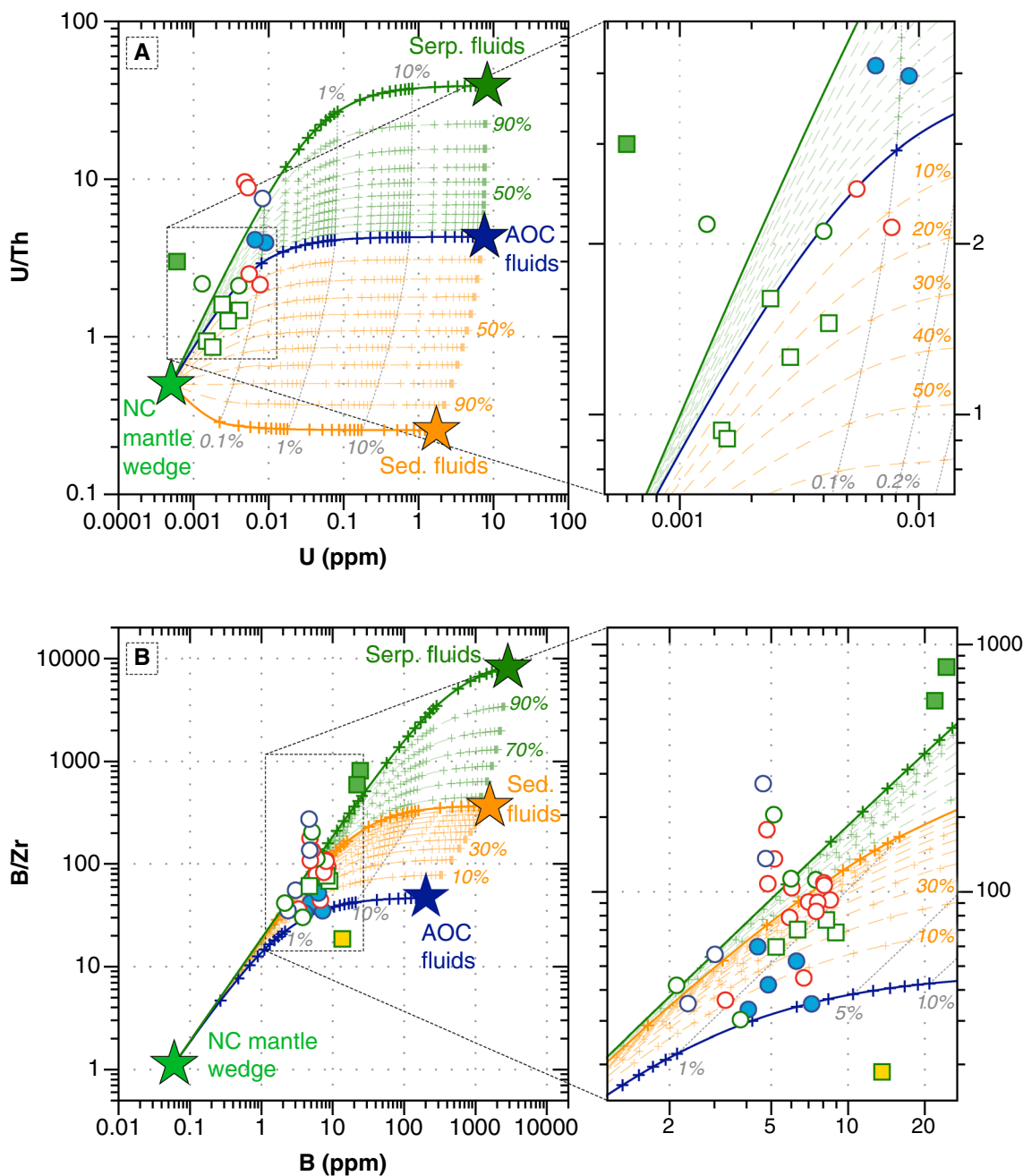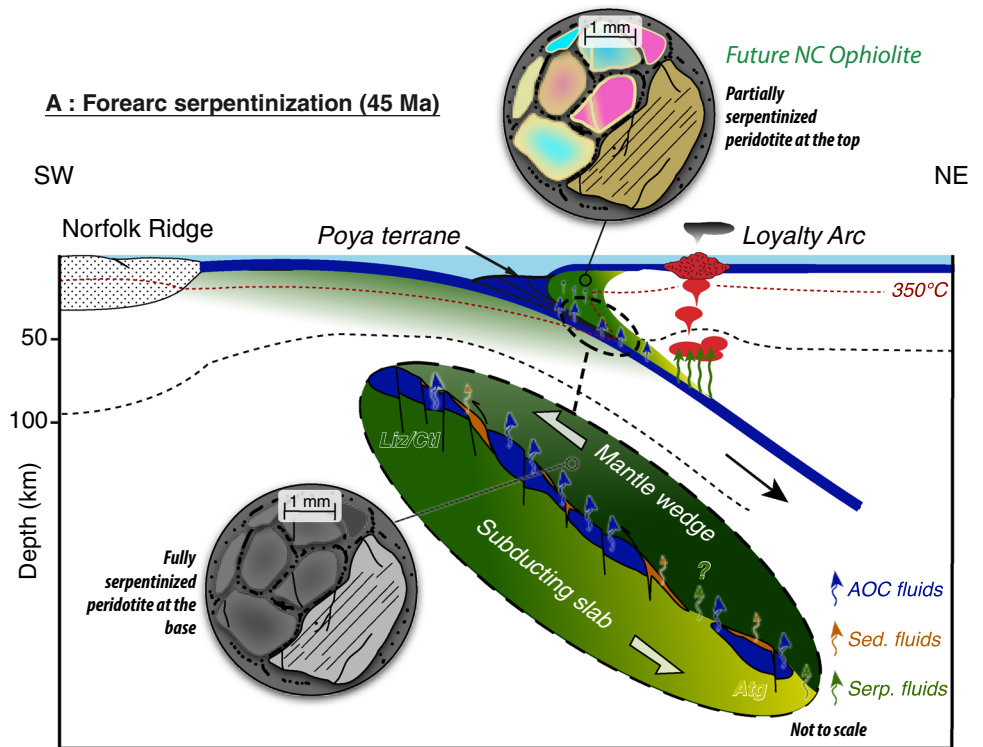The development of multiple serpentine generations in the tectonic sole likely reflects changes in crystallization

Fig. 9 Plots of **a** U/Th vs. U and **b** B/Zr vs. B of NC serpentines. Thick solid lines represent the bulk mixing between the NC mantle wedge and sediment-derived fluids (in orange), with AOC-derived fluids (in blue) and with serpentine-derived fluids (in green). Thin dotted lines represent the bulk mixing between the NC mantle wedge and AOC-derived fluids mixed with various amounts of sediment-derived fluids (in orange) and serpentine-derived fluids (in green). Grey dotted lines correspond to the percentage additions of slab-derived fluids to the mantle wedge. Compositions of the NC mantle wedge and AOC, sediment and serpentine-derived fluids and respective sources are listed in Table 4

conditions, including the fluid composition and the formation events, both being connected with the tectonic history of the Peridotite Nappe. Consistently, the significant differences in the chemical compositions from S1 to S2

serpentines (e.g., increasing Mg#, different trace element patterns) may reveal a change in the elemental budget of serpentinizing fluids. On the other hand, the transition from the lizardite–antigorite assemblage (S2–S3/S4) to

Fig. 10 a A simple model for the serpentinization of the New Caledonia ophiolite. **a** Massive hydration of the forearc mantle related to the dehydration of the altered oceanic basement of the subducted plate, leading to the formation of fully serpentinized peridotites (including pyroxenes) at the slab interface, where fluid flows are the most intense, and partially serpentinized peridotites at shallower depths where fluid flows are less expressed. **b** Conceptual model of the serpentinite sole formation in response to the percolation of meteoric fluids at the base of the NC ophiolite during its emplacement on the Norfolk continental basement. Note that these meteoric fluids previously interacted with peridotite the top of the ophiolite, forming a thick regolith since the ophiolite emersion at 34 Ma. (modified after Lagabrielle et al. 2013). The legend is the same as in Fig. 1
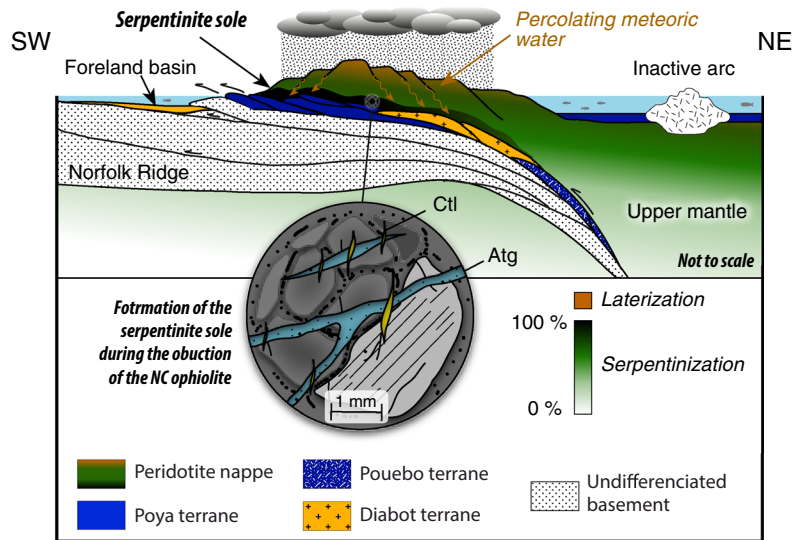
chrysotile–polygonal serpentine (S5–S6) without significant changes in the serpentine chemistry is in favour of a sole development under cooling temperatures. Our modeling approach of stable isotopes suggests that AOC-derived fluids alone cannot explain the formation of the serpentinite sole. Low temperature fluids (~ 100–250 °C) of a meteoric origin can be considered (Fig. 8b). The involvement of meteoric fluids is also suggested by major and trace element compositions of sole serpentines. The high Fe^{3+}/Fe_T ratio in

serpentines from the sole (Fig. 5) indicates a formation under more oxidizing conditions than in the upper system, which may be interpreted in term of formation depth.

Interestingly, Muñoz et al. (2019) showed that secondary serpentines, which are formed close to the surface by the circulation of meteoric fluids during the early stages of laterization display an increasing amount of ferric iron from lizardite ($Fe^{3+}/Fe_T = 0.4$) to polygonal serpentine ($Fe^{3+}/Fe_T = 0.95$). Fe^{3+}/Fe_T ratios in serpentines from the

sole are very comparable to those measured in the regolith. Polygonal serpentine was also the latest serpentine variety to form and it has the highest Fe^{3+}/Fe_T. We thus interpret the increase of ferric iron in serpentines from the sole as evidence of their formation under near-surface conditions (i.e., low temperature, high fO_2). The behavior of LREE provides additional proof of meteoric fluid involvement in the formation of the serpentinite sole. Serpentines from the serpentinite sole are LREE-enriched, except Ce. The exact opposite, i.e., LREE depletion and strong Ce positive anomaly (Fig. 7), is observed in laterites on top of the NC regolith and is explained by the very low mobility of Ce^{4+} relative to all other REE (Ulrich et al. 2019). Also, the downslope migration of elements from the regolith can explain the high U/Th ratio in serpentines from the sole. Indeed, U is mobile under oxidizing surface conditions, while Th is insoluble (e.g., Dequincey et al. 2002). As a consequence, U/Th ratio is lower in laterites than in the initial peridotite (Fig. 7). Meteoric fluids may thus transport LREE, and potentially other FME, released during weathering. A high U/Th ratio and a low Ce/Ce* ratio in serpentine is therefore not necessarily a marker for the influence of seawater solely.

Lateritization has been considered as rather early and was active during or slightly after the ophiolite emplacement by Quesnel et al. (2013), based on a coupled isotopic and structural analysis of magnesite veins. Following our Monte-Carlo simulations, the O and H isotope signatures of the meteoric fluids involved during serpentinization ($\delta^{18}O = -6 \pm 2‰$, $\delta D = -40 \pm 10‰$; Fig. 8b) are comparable with present-day rainwater (Nicolini et al. 2016). The current discharge of H_2, CH_4, and N_2-enriched hyperalkaline spring waters reveals active and low-temperature serpentinization at the base of the NC ophiolite (Deville and Prinzhofer 2016; Monnin et al. 2014). Thus, the serpentinization of the serpentinite sole was partly formed in response to the circulation of meteoric fluids during the late stages of its emplacement (Fig. 10b). After the crystallization of lizardite 2 in microfracture networks, antigorite veins may have crystallized under moderate temperatures (< 250 °C), and high deformation conditions, such as documented by Ribeiro Da Costa et al. (2008). Finally, as the obduction proceeded, the progressive cooling temperatures may have led to the replacement of antigorite into lower temperature species, such as chrysotile and polygonal serpentine, as shown by Quesnel et al. (2016b).

Conclusions

The new mineralogical and geochemical data presented here, on the serpentinites from the peridotite nappe and the sole of NC ophiolite, provide evidence for a polyphasic history of fluid–rock interactions. Using trace element concentrations

and a new modeling approach based on Monte Carlo simulations applied on oxygen and hydrogen isotope compositions, we propose that the main serpentinization event (lizardite formation) mostly occurred during the NE-dipping subduction in the SLB due to slab dehydration and subsequent hydration of forearc mantle wedge (i.e., the future Peridotite Nappe). Also, our simulations shift serpentinization temperatures in the fore-arc mantle in the range of 250–450 °C, with an upper threshold that may be lowered to ~ 350 °C, as inferred by the lack of antigorite.

Other serpentine species present in the serpentinite sole recorded retrogression during fore-arc cooling and obduction. These serpentinization events occurred under high strain conditions and at lower temperature, from ~ 250 °C to < 100 °C. From the oxygen and hydrogen isotope composition of these serpentines, we suggest a meteoric contribution for the late stage serpentinizing fluids. Thus, this study demonstrates that serpentine in ophiolite may record a long history of fluid–rock interactions, from early fluid circulations deep into the forearc mantle to late meteoric fluid percolation at shallow depth during obduction.

References

Agard P, Yamato P, Soret M, Prigent C, Guillot S, Plunder A, Dubacq B, Chauvet A, Monié P (2016) Plate interface rheological switches during subduction infancy: control on slab penetration and metamorphic sole formation. Earth Planet Sci Lett 451:208–220

Agrinier P, Cannat M (1997) Oxygen-isotope constraints on serpentinization processes in ultramafic rocks from the Mid-Atlantic Ridge(23 °N). Proc Ocean Drill Program Sci Results 153:381–388

Agrinier P, Hékinian R, Bideau D, Javoy M (1995) O and H stable isotope compositions of oceanic crust and upper mantle rocks exposed in the Hess Deep near the Galapagos Triple Junction. Earth Planet Sci Lett 136(3–4):183–196

Aitchison JC, Clarke GL, Meffre S, Cluzel D (1995) Eocene arc-continent collision in New Caledonia and implications for regional southwest Pacific tectonic evolution. Geology 23(2):161

Aizawa Y, Tatsumi Y, Yamada H (1999) Element transport by dehydration of subducted sediments: implication for arc and ocean island magmatism. Island Arc 8(1):38–46

Alt JC (2003) Stable isotopic composition of upper oceanic crust formed at a fast spreading ridge, ODP Site 801. Geochem Geophys Geosyst 4(5):8908. https://doi.org/10.1029/2002GC000400

Alt JC, Shanks WC III (2003) Serpentinization of abyssal peridotites from the MARK area, Mid-Atlantic Ridge: sulfur geochemistry and reaction modeling. Geochim Cosmochim Acta 67(4):641–653

Alt JC, Shanks WC III (2006) Stable isotope compositions of serpentinite seamounts in the Mariana forearc: serpentinization processes, fluid sources and sulfur metasomatism. Earth Planet Sci Lett 242(3):272–285

Alt JC, Shanks WC, Bach W, Paulick H, Garrido CJ, Beaudoin G (2007) Hydrothermal alteration and microbial sulfate reduction in peridotite and gabbro exposed by detachment faulting at the Mid-Atlantic Ridge, 15°20′N (ODP Leg 209): a sulfur and oxygen isotope study. Geochem Geophys Geosyst 8:Q08002. https://doi.org/10.1029/2007GC001617

Alt JC, Garrido CJ, Shanks WC III, Turchyn A, Padrón-Navarta JA, Sánchez-Vizcaíno VL, Pugnaire MTG, Marchesi C (2012) Recycling of water, carbon, and sulfur during subduction of serpentinites: a stable isotope study of Cerro del Almirez, Spain. Earth Planet Sci Lett 327–328:1–11

Andréani M, Mével C, Boullier AM, Escartin J (2007) Dynamic control on serpentine crystallization in veins: constraints on hydration processes in oceanic peridotites. Geochem Geophys Geosyst 8(2):24

Andréani M, Escartin J, Delacour A, Ildefonse B, Godard M, Dyment J, Fallick AE, Fouquet Y (2014) Tectonic structure, lithology, and hydrothermal signature of the Rainbow massif (Mid-Atlantic Ridge 36° 14′ N). Geochem Geophys Geosyst 15(9):3543–3571

Auzende AL, Daniel I, Reynard B, Lemaire C, Fo G (2004) High-pressure behaviour of serpentine minerals: a Raman spectroscopic study. Phys Chem Miner 31(5):269–277

Avias J (1967) Overthrust structure of the main ultrabasic new caledonian massives. Tectonophysics 4(4–6):531–541

Bailey EH, Ragnarsdottir KV (1994) Uranium and thorium solubilities in subduction zone fluids. Earth Planet Sci Lett 124(1–4):119–129

Bali E, Audétat A, Keppler H (2010) The mobility of U and Th in subduction zone fluids: an indicator of oxygen fugacity and fluid salinity. Contrib Mineral Petrol 161(4):597–613

Beard JS, Frost BR (2017) The stoichiometric effects of ferric iron substitutions in serpentine from microprobe data. Int Geol Rev 59(5–6):541–547

Bonatti E, Lawrence JR, Morandi N (1984) Serpentinization of oceanic peridotites: temperature dependence of mineralogy and boron content. Earth Planet Sci Lett 70:88–94

Brenan JM, Shaw HF, Ryerson FJ, Phinney DL (1995) Mineral-aqueous fluid partitioning of trace elements at 900°C and 2.0 GPa: constraints on the trace element chemistry of mantle and deep crustal fluids. Geochim Cosmochim Acta 59(16):3331–3350

Burkhard DJM, O'Neil JR (1988) Contrasting serpentinization processes in the eastern Central Alps. Contrib Mineral Petrol 99(4):498–506

Cannat M, Mevel C, Maia M, Deplus C, Durand C, Gente P, Agrinier P, Belarouchi A, Dubuisson G, Humler E (1995) Thin crust, ultramafic exposures, and rugged faulting patterns at the Mid-Atlantic Ridge (22–24°N). Geology 23(1):49–52

Cathelineau M, Quesnel B, Gautier P, Boulvais P, Couteau C, Drouillet M (2015) Nickel dispersion and enrichment at the bottom of the regolith: formation of pimelite target-like ores in rock block joints (Koniambo Ni deposit, New Caledonia). Miner Deposita 51(2):271–282

Cathelineau M, Myagkiy A, Quesnel B, Boiron M-C, Gautier P, Boulvais P, Ulrich M, Truche L, Golfier F, Drouillet M (2016) Multistage crack seal vein and hydrothermal Ni enrichment in serpentinized ultramafic rocks (Koniambo massif, New Caledonia). Miner Deposita 52(7):1–16

Chen JH, Edwards RL, Wasserburg GJ (1986) 238U,234U and232Th in seawater. Earth Planet Sci Lett 80(3–4):241–251

Chenin P, Manatschal G, Picazo S, Müntener O, Karner G, Johnson C, Ulrich M (2017) Influence of the architecture of magma-poor hyperextended rifted margins on orogens produced by the closure of narrow versus wide oceans. Geosphere 13(2):559–576. https://doi.org/10.1130/GES01363.1

Cluzel D, Picard C, Aitchison JC, Laporte C, Meffre S, Parat F (1997) La nappe de Poya (ex-formation des Basaltes) de Nouvelle-Calédonie (Pacifique Sud-Ouest): un plateau océanique Campanien-Paléocène supérieur obducté à l'Eocène supérieur. CR Acad Sci Paris 324(6):443–451

Cluzel D, Chiron D, Courme M-D (1998) Discordance de l'Éocène supérieur et événements pré-obduction en Nouvelle-Calédonie. Comptes Rendus de l'Académie des Sciences - Series IIA - Earth and Planetary Science 327(7):485–491

Cluzel D, Aitchison JC, Picard C (2001) Tectonic accretion and underplating of mafic terranes in the Late Eocene intraoceanic fore-arc of New Caledonia (Southwest Pacific): geodynamic implications. Tectonophysics 340(1–2):23–59

Cluzel D, Meffre S, Maurizot P, Crawford AJ (2006) Earliest Eocene (53 Ma) convergence in the Southwest Pacific: evidence from pre-obduction dikes in the ophiolite of New Caledonia. Terra Nova 18(6):395–402

Cluzel D, Jourdan F, Meffre S, Maurizot P, Lesimple S (2012a) The metamorphic sole of New Caledonia ophiolite: 40Ar/39Ar, U-Pb, and geochemical evidence for subduction inception at a spreading ridge. Tectonics 31(3):3016

Cluzel D, Maurizot P, Collot J (2012b) An outline of the Geology of New Caledonia; from Permian-Mesozoic Southeast Gondwanaland active margin to Cenozoic obduction and supergene evolution. Episodes 35(1):72–86

Cluzel D, Ulrich M, Jourdan F, Meffre S, Paquette J-L, Audet M-A, Secchiari A, Maurizot P (2016) Early Eocene clinoenstatite boninite and boninite-series dikes of the ophiolite of New Caledonia; a witness of slab-derived enrichment of the mantle wedge in a nascent volcanic arc. Lithos 260:429–442

Cluzel D, Whitten M, Meffre S, Aitchison JC, Maurizot P (2018) A Reappraisal of the Poya Terrane (New Caledonia): accreted Late Cretaceous-Paleocene Marginal Basin Upper Crust, Passive Margin Sediments, and Early Eocene E-MORB Sill Complex. Tectonics 37(1):48–70

Cluzel D, Boulvais P, Iseppi M, Lahondère D, Lesimple S, Maurizot P, Paquette J, Tarantola A, Ulrich M (2019) Slab-derived origin of tremolite–antigorite veins in a supra-subduction ophiolite: the Peridotite Nappe (New Caledonia) as a case study International Journal of Earth Sciences 109(1):171–196. https://doi.org/10.1007/s00531-019-01796-6

Debret B, Andréani M, Godard M, Nicollet C, Schwartz S, Lafay R (2013) Trace element behavior during serpentinization/de-serpentinization of an eclogitized oceanic lithosphere: a LA-ICPMS study of the Lanzo ultramafic massif (Western Alps). Chem Geol 357:117–133

Delacour A, Früh-Green GL, Frank M, Gutjahr M, Kelley DS (2008) Sr- and Nd-isotope geochemistry of the Atlantis Massif (30°N, MAR): implications for fluid fluxes and lithospheric heterogeneity. Chem Geol 254(1–2):19–35

Deloule E, Albarede F, Sheppard SMF (1991) Hydrogen isotope heterogeneities in the mantle from ion probe analysis of amphiboles from ultramafic rocks. Earth Planet Sci Lett 105(4):543–553

Dequincey O, Chabaux F, Clauer N, Sigmarsson O, Liewig N, Leprun JC (2002) Chemical mobilizations in laterites: evidence from trace elements and 238U–234U-230Th disequilibria. Geochim Cosmochim Acta 66(7):1197–1210

Deschamps F (2010) Caractérisation in situ des serpentines en contexte de subduction: De la nature à l'expérience, Thesis, Université Joseph Fourier, Grenoble, p 308

Deschamps F, Guillot S, Godard M, Andréani M, Hattori KH (2011) Serpentinites act as sponges for fluid-mobile elements in abyssal and subduction zone environments. Terra Nova 23(3):171–178

Deschamps F, Godard M, Guillot S, Chauvel C, Andréani M, Hattori KH, Wunder B, France L (2012) Behavior of fluid-mobile elements in serpentines from abyssal to subduction environments: examples from Cuba and Dominican Republic. Chem Geol 312–313:93–117

Deschamps F, Godard M, Guillot S, Hattori KH (2013) Geochemistry of subduction zone serpentinites: a review. Lithos 178:96–127

Deville E, Prinzhofer A (2016) The origin of N2-H2-CH4-rich natural gas seepages in ophiolitic context: a major and noble gases study of fluid seepages in New Caledonia. Chem Geol 440:139–147

Eiler JM (2001) Oxygen isotope variations of basaltic lavas and upper mantle rocks. Stable Isotope Geochem 43:319–364

Eiler JM, McInnes B, Valley JW, Graham CM, Stolper EM (1998) Oxygen isotope evidence for slab-derived fluids in the sub-arc mantle. Nature 393(6687):777–781

Eissen J-P, Crawford AJ, Cotten J, Meffre S, Bellon H, Delaune M (1998) Geochemistry and tectonic significance of basalts in the Poya Terrane. New Caledonia Tectonophys 284(3–4):203–219

Elderfield H, Greaves MJ (1982) The rare earth elements in seawater. Nature 296(5854):214–219

Evans B, Johannes W, Oterdoom H, Trommsdorff V (1976) Stability of chrystotile and antigorite in the serpentine multisystem. Schweiz Mineral Petrogr Mitt 56:79–93

Evans BW (2004) The serpentinite multisystem revisited: chrysotile is metastable. Int Geol Review 46(6):479–506

Frisby C, Bizimis M, Mallick S (2016) Seawater-derived rare earth element addition to abyssal peridotites during serpentinization. Lithos 248–251:432–454

Fritsch E, Juillot F, Dublet G, Fonteneau L, Fandeur D, Martin E, Caner L, Auzende AL, Grauby O, Beaufort D (2016) An alternative model for the formation of hydrous Mg/Ni layer silicates ('deweylite'/'garnierite') in faulted peridotites of New Caledonia: I. Texture and mineralogy of a paragenetic succession of silicate infillings. Eur J Mineral 28(2):295–311

Frost BR, Evans KA, Swapp SM, Beard JS, Mothersole FE (2013) The process of serpentinization in dunite from New Caledonia. Lithos 178:24–39

Früh-Green G, Plas A, Lécuyer C (1996) Petrologic and stable isotope constraints on hydrothermal alteration and serpentinization of the EPR shallow mantle at Hess Deep(Site 895). Proc ODP Sci Results 147:255–291

Früh-Green G, Scambelluri M, Vallis F (2001) OH isotope ratios of high pressure ultramafic rocks: implications for fluid sources and mobility in the subducted hydrous mantle. Contrib Miner Petrol 141(2):145–159

Fryer P (1992) A synthesis of Leg 125 drilling of serpentine seamounts on the Mariana and Izu-Bonin forearcs. In: vol Fryer P, Pearce JA, Stokking LB et al (eds) Proceedings of the ODP, Science Results, 125: College Station, TX (Ocean Drilling Program) pp 593–614

Gautier P, Quesnel B, Boulvais P, Cathelineau M (2016) The emplacement of the Peridotite Nappe of New Caledonia and its bearing on the tectonics of obduction. Tectonics 35(12):3070–3094

Gillard M, Tugend J, Müntener O, Manatschal G, Karner G, Autin J, Sauter D, Figueredo PH, Ulrich M (2019) The role of serpentinization and magmatism in the formation of decoupling interfaces at magma-poor rifted margins. Earth-Sci Rev 196:102882

Guillot S, Hattori KH, de Sigoyer J (2000) Mantle wedge serpentinization and exhumation of eclogites: insights from eastern Ladakh, northwest Himalaya. Geology 28(3):199

Guillot S, Hattori KH, Agard P, Schwartz S, Vidal O (2009) Exhumation processes in oceanic and continental subduction contexts: a review. Subduction zone geodynamics. Springer, New York, pp 175–205

Guillot S, Schwartz S, Reynard B, Agard P, Prigent C (2015) Tectonic significance of serpentinites. Tectonophysics 646:1–19

Hattori KH, Guillot S (2003) Volcanic fronts form as a consequence of serpentinite dehydration in the forearc mantle wedge. Geology 31(6):525–528

Hattori KH, Guillot S (2007) Geochemical character of serpentinites associated with high- to ultrahigh-pressure metamorphic rocks in the Alps, Cuba, and the Himalayas: recycling of elements in subduction zones. Geochem Geophys Geosyst 8(9):Q09010. https://doi.org/10.1029/2007GC001594

Hoefs J (2009) Stable isotope geochemistry. Springer, Berlin

Hyndman RD, Peacock SM (2003) Serpentinization of the forearc mantle. Earth Planet Sci Lett 212(3–4):417–432

Iwamori H (1998) Transportation of H2O and melting in subduction zones. Earth Planet Sci Lett 160(1):65–80

Iyer K, Austrheim H, John T, Jamtveit B (2008) Serpentinization of the oceanic lithosphere and some geochemical consequences: constraints from the Leka Ophiolite Complex. Norway Chem Geol 249(1–2):66–90

Klein F, Bach W, McCollom TM (2013) Compositional controls on hydrogen generation during serpentinization of ultramafic rocks. Lithos 178:55–69

Klein F, Marschall HR, Bowring SA, Humphris SE, Horning G (2017) Mid-ocean ridge serpentinite in the Puerto Rico Trench: from seafloor spreading to subduction. J Petrology 58(9):1729–1754

Kodolanyi J, Pettke T, Spandler C, Kamber BS, Gmeling K (2012) Geochemistry of ocean floor and fore-arc serpentinites: constraints on the ultramafic input to subduction zones. J Petrol 53(2):235–270

Kogiso T, Tatsumi Y, Nakano S (1997) Trace element transport during dehydration processes in the subducted oceanic crust: 1. Experiments and implications for the origin of ocean island basalts. Earth Planet Sci Lett 148(1–2):193–205

Kyser TK, O'Hanley DS, Wicks FJ (1999) The origin of fluids associated with serpentinization processes: evidence from stable-isotope compositions. Can Mineral 37(1):223–237

Lafay R, Deschamps F, Schwartz S, Guillot S, Godard M, Debret B, Nicollet C (2013) High-pressure serpentinites, a trap-and-release system controlled by metamorphic conditions: example from the Piedmont zone of the western Alps. Chem Geol 343:38–54

Lemaire C (2000) Application des spectroscopies vibrationnelles à la détection d'amiante dans les matériaux et à l'étude des serpentines. Université de Paris 7

Longerich HP, Jackson SE, Günther D (1996) Laser ablation inductively coupled plasma mass spectrometric transient signal data acquisition and analyte concentration calculation. J Anal At Spectrom 11(9):899–904

Magaritz M, Taylor HP (1974) Oxygen and hydrogen isotope studies of serpentinization in the Troodos ophiolite complex. Cyprus Earth Planet Sci Lett 23(1):8–14

McDonough WF, Sun SS (1995) The composition of the Earth. Chem Geol 120(3–4):223–253

McRae ME (2020) Nickel. In: U.S. Geological Survey, 2020, Mineral commodity summaries pp 112–113.https://doi.org/10.3133/mcs2020

Mével C (2003) Serpentinization of abyssal peridotites at mid-ocean ridges. Comptes Rendus Geosci 335(10–11):825–852

Monnin C, Chavagnac V, Boulart C, Ménez B, Gérard M, Gérard E, Pisapia C, Quéméneur M, Erauso G, Postec A, Guentas-Dombrowski L, Payri C, Pelletier B (2014) Fluid chemistry of the low temperature hyperalkaline hydrothermal system of Prony Bay (New Caledonia). Biogeosciences 11(20):5687–5706

Mothersole FE, Evans K, Frost BR (2017) Abyssal and hydrated mantle wedge serpentinised peridotites: a comparison of the 15°20'N fracture zone and New Caledonia serpentinites. Contrib Mineral Petrol 172(8):69

Muñoz M, Ulrich M, Cathelineau M, Mathon O (2019) Weathering processes and crystal chemistry of Ni-bearing minerals in saprock horizons of New Caledonia ophiolite. J Geochem Explor 198:82–99

Nicolini E, Rogers K, Rakowski D (2016) Baseline geochemical characterisation of a vulnerable tropical karstic aquifer; Lifou, New Caledonia. Biochem Pharmacol 5:114–130

O'Hanley DS (1996) Serpentinites: records of tectonic and petrological history. Oxford University Press, Oxford

Orloff O (1968) Etude geologique et geomorphologique des massifs d'ultrabasites compris entre Houailou et Canala (Nouvelle-Caledonie)

Peacock SM (1990) Fluid processes in subduction zones. Science 248(4):329–337

Peacock SM, Hyndman RD (1999) Hydrous minerals in the mantle wedge and the maximum depth of subduction thrust earthquakes. Geophys Res Lett 26(16):2517–2520

Pearce NJG, Perkins WT, Westgate JA, Gorton MP, Jackson SE, Neal CR, Chenery SP (1997) A Compilation of new and published major and trace element data for NIST SRM 610 and NIST SRM 612 glass reference materials. Geostand Geoanal Res 21(1):115–144

Peters D, Bretscher A, John T, Scambelluri M, Pettke T (2017) Fluid-mobile elements in serpentinites: constraints on serpentinisation environments and element cycling in subduction zones. Chem Geol 466:654–666

Picazo S, Cannat M, Delacour A, Escartín J, Rouméjon S, Silantyev S (2012) Deformation associated with the denudation of mantle-derived rocks at the Mid-Atlantic Ridge 13°–15°N: The role of magmatic injections and hydrothermal alteration. Geochem Geophys Geosyst 13(9):Q04G09. https://doi.org/10.1029/2012GC004121

Pinto VHG, Manatschal G, Karpoff AM, Ulrich M, Viana AR (2016) Seawater storage and element transfer associated with mantle serpentinization in magma-poor rifted margins: a quantitative approach. Earth Planet Sci Lett 459:1–11

Pirard C, Hermann J, O'Neill HSC (2013) Petrology and Geochemistry of the Crust-Mantle Boundary in a Nascent Arc, Massif du Sud Ophiolite, New Caledonia. SW Pac J Petrol 54(9):1759–1792

Plank T (2014) The chemical composition of subducted sediments. Treatise on geochemistry, vol 4. Elsevier, Amsterdam, pp 607–629

Poli S, Schmidt MW (2002) Petrology of subducted slabs. Ann Rev Earth Planet Sci 30(1):207–235

Quesnel B, Boulvais P, Gautier P, Cathelineau M, Maurizot P, Cluzel D, Ulrich M, Guillot S, Lesimple S, Couteau C (2013) Syn-tectonic, meteoric water-derived carbonation of the New Caledonia peridotite nappe. Geology 41(10):1063–1066

Quesnel B, Boulvais P, Gautier P, Cathelineau M, John CM, Dierick M, Agrinier P, Drouillet M (2016a) Paired stable isotopes (O, C) and clumped isotope thermometry of magnesite and silica veins in the New Caledonia Peridotite Nappe. Geochim Cosmochim Acta 183:234–249

Quesnel B, Gautier P, Cathelineau M, Boulvais P, Couteau C, Drouillet M (2016b) The internal deformation of the Peridotite Nappe of New Caledonia: a structural study of serpentine-bearing faults and shear zones in the Koniambo Massif. J Struct Geol 85:51–67

Reynard B (2013) Serpentine in active subduction zones. Lithos 178:171–185

Ribeiro Da Costa I, Barriga FJAS, Viti C, Mellini M, Wicks FJ (2008) Antigorite in deformed serpentinites from the Mid-Atlantic Ridge. Eur J Mineral 20:563–572

Rouméjon S, Cannat M, Agrinier P, Godard M, Andréani M (2015) Serpentinization and fluid pathways in tectonically exhumed peridotites from the southwest Indian Ridge (62–65 E). J Petrol 56(4):703–734

Rüpke LH, Morgan JP, Hort M, Connolly JAD (2004) Serpentine and the subduction zone water cycle. Earth Planet Sci Lett 223(1–2):17–34

Saccocia PJ, Seewald JS, Shanks WC III (2009) Oxygen and hydrogen isotope fractionation in serpentine–water and talc–water systems from 250 to 450°C, 50 MPa. Geochim Cosmochim Acta 73(22):6789–6804

Sakai H, Tsutsumi M (1978) D-H fractionation factors between serpentine and water at 100°C to 500°C and 2000 bar water-pressure, and D-H ratios of natural serpentines. Earth Planet Sci Lett 40(2):231–242

Sakai R, Kusakabe M, Noto M, Ishii T (1990) Origin of waters responsible for serpentinization of the Izu-Ogasawara-Mariana forearc seamounts in view of hydrogen and oxygen isotope ratios. Earth Planet Sci Lett 100(1–3):291–303

Salters VJM, Longhi JE, Bizimis M (2002) Near mantle solidus trace element partitioning at pressures up to 3.4 GPa. Geochem Geophys Geosyst 3(7):1–23

Salters VJM, Stracke A (2004) Composition of the depleted mantle. Geochem Geophys Geosyst 5(5):Q05B07. https://doi.org/10.1029/2003GC000597

Sano T, Hasenaka T, Shimaoka A, Yonezawa C, Fukuoka T (2001) Boron contents of Japan Trench sediments and Iwate basaltic lavas, Northeast Japan arc: estimation of sediment-derived fluid contribution in mantle wedge. Earth Planet Sci Lett 186(2):187–198

Savin SM, Lee M (1988) Isotopic studies of phyllosilicates. In: Bailey S (ed) Hydrous Phyllosilicates (exclusive of micas), vol 19. Mineralogical Society of America, Chantilly, pp 189–223

Savov IP, Ryan J, D'Antonio M, Kelley K, Mattie P (2005) Geochemistry of serpentinized peridotites from the Mariana Forearc Conical Seamount, ODP Leg 125: implications for the elemental recycling at subduction zones. Geochem Geophys Geosyst 6(4);Q04J1. https://doi.org/10.1029/2004GC000777

Scambelluri M, Fiebig J, Malaspina N, Müntener O, Pettke T (2004) Serpentinite subduction: implications for fluid processes and trace-element recycling. Int Geol Rev 46:595–613

Schmidt MW, Poli S (1998) Experimentally based water budgets for dehydrating slabs and consequences for arc magma generation. Earth Planet Sci Lett 163(1):361–379

Schwartz S, Allemand P, Guillot S (2001) Numerical model of the effect of serpentinites on the exhumation of eclogitic rocks: insights from the Monviso ophiolitic massif (Western Alps). Tectonophysics 342(1–2):193–206

Schwarzenbach EM, Caddick MJ, Beard JS, Bodnar RJ (2015) Serpentinization, element transfer, and the progressive development of zoning in veins: evidence from a partially serpentinized harzburgite. Contrib Miner Petrol 171(1):1–22

Secchiari A, Montanini A, Bosch D, Macera P, Cluzel D (2016) Melt extraction and enrichment processes in the New Caledonia lherzolites: evidence from geochemical and Sr–Nd isotope data. Lithos 260:28–43

Secchiari A, Montanini A, Bosch D, Macera P, Cluzel D (2019) Sr, Nd, Pb and trace element systematics of the New Caledonia

harzburgites: tracking source depletion and contamination processes in a SSZ setting. Geosci Front 11:37–55

Sharp Z (1992) In situ laser microprobe techniques for stable isotope analysis. Chem Geol 101:3–19

Sharp Z, Atudorei V, Durakiewicz T (2001) A rapid method for determination of hydrogen and oxygen isotope ratios from water and hydrous minerals. Chem Geol 178(1–4):197–210

Sheppard SMF, Nielsen RL, Taylor HP (1969) Oxygen and hydrogen isotope ratios of clay minerals from porphyry copper deposits. Econ Geol 64(7):755–777

Smith H, Spivack A, Staudigel H, Hart S (1995) The boron isotopic composition of altered oceanic crust. Chem Geol126(2):119–135. https://doi.org/10.1016/0009-2541(95)00113-6

Staudigel H, Hart SR, Richardson SH (1981) Alteration of the oceanic crust: processes and timing. Earth Planet Sci Lett 52(2):311–327

Staudigel H, Plank T, White B, Schmincke H (1996) Geochemical fluxes during seafloor alteration of the basaltic upper oceanic Crust: DSDP sites 417 and 418, in Subduction Top to Bottom. 96:19–38. https://doi.org/10.1029/gm096p0019

Stern RJ (2002) Subduction zones. Rev Geophys 40(4):1012

Tenthorey E, Hermann J (2004) Composition of fluids during serpentinite breakdown in subduction zones: evidence for limited boron mobility. Geology 32(1):865

Thakurta J, Ripley EM, Li C (2009) Oxygen isotopic variability associated with multiple stages of serpentinization, Duke Island Complex, southeastern Alaska. Geochim Cosmochim Acta 73(20):6298–6312

Ulmer P, Trommsdorff V (1995) Serpentine stability to mantle depths and subduction-related magmatism. Science 268(5212):858–861

Ulmer P, Trommsdorff V (1999) Phase relations of hydrous mantle subducting to 300km. Geochem Soc Spec Publ 6:259–281

Ulrich M, Picard C, Guillot S, Chauvel C, Cluzel D, Meffre S (2010) Multiple melting stages and refertilization as indicators for ridge to subduction formation: the New Caledonia ophiolite. Lithos 115(1):223–236

Ulrich M, Muñoz M, Guillot S, Cathelineau M, Picard C, Quesnel B, Boulvais P, Couteau C (2014) Dissolution–precipitation processes governing the carbonation and silicification of the serpentinite sole of the New Caledonia ophiolite. Contrib Miner Petrol 167(1):952–1019

Ulrich M, Cathelineau M, Muñoz M, Boiron M-C, Teitler Y, Karpoff AM (2019) The relative distribution of critical (Sc, REE) and transition metals (Ni Co, Cr, Mn, V) in some Ni-laterite deposits of New Caledonia. J Geochem Explor 197:93–113

Wenner D, Taylor H (1971) Temperatures of serpentinization of ultramafic rocks based on O 18/O 16 fractionation between coexisting serpentine and magnetite. Contrib Miner Petrol 32(3):165–185

Wenner DB, Taylor HP (1973) Oxygen and hydrogen isotope studies of the serpentinization of ultramafic rocks in oceanic environments and continental ophiolite complexes. Am J Sci 273(3):207

Whattam SA, Malpas J, Ali JR, Smith IEM (2008) New SW Pacific tectonic model: cyclical intraoceanic magmatic arc construction and near-coeval emplacement along the Australia-Pacific margin in the Cenozoic. Geochem Geophys Geosyst 9(3):Q03021. https://doi.org/10.1029/2007GC001710

Workman RK, Hart SR (2005) Major and trace element composition of the depleted MORB mantle (DMM). Earth Planet Sci Lett 231(1–2):53–72

Wunder B, Wirth R, Gottschalk M (2001) Antigorite: pressure and temperature dependence of polysomatism and water content. Eur J Mineral 13(3):485

Zheng Y (1993) Calculation of oxygen-isotope fractionation in hydroxyl-bearing silicates. Earth Planet Sci Lett 120:247–263